AGU PUBLICATIONS

JGR

Journal of Geophysical Research: Oceans

RESEARCH ARTICLE

10.1002/2015JC011155

Uniform asymptotic approximations for transient waves due to an initial disturbance

Per A. Madsen[1], Hemming A. Schäffer[2], David R. Fuhrman[1], and Yaron Toledo[3]

[1]Department of Mechanical Engineering, Technical University of Denmark, Kgs Lyngby, Denmark, [2]SchäfferWaves, Copenhagen Ø, Denmark, [3]School of Mechanical Engineering, Faculty of Engineering, Tel Aviv University, Israel

Key Points:
- A mathematical model for transient waves due to an initial disturbance is developed
- Uniform asymptotic approximations are combined with efficient convolution methods in 2-D and 3-D
- The model provides fast solutions for the evolution of tsunamis

Correspondence to:
P. A. Madsen,
prmr@mek.dtu.dk

Citation:
Madsen, P. A., H. A. Schäffer, D. R. Fuhrman, and Y. Toledo (2015), Uniform asymptotic approximations for transient waves due to an initial disturbance, *J. Geophys. Res. Oceans*, *120*, doi:10.1002/2015JC011155.

Received 23 JUL 2015
Accepted 26 NOV 2015
Accepted article online 8 DEC 2015

Abstract In this work, we first present a semianalytical method for the evolution of linear fully dispersive transient waves generated by an initial surface displacement and propagating over a constant depth. The procedure starts from Fourier and Hankel transforms and involves a combination of the method of stationary phase, the method of uniform asymptotic approximations and various Airy integral formulations. Second, we develop efficient convolution techniques expressed as single and double summations over the source area. These formulations are flexible, extremely fast, and highly accurate even for the dispersive tail of the transient waves. To verify the accuracy of the embedded dispersion properties, we consider test cases with sharp-edged disturbances in 1-D and 2-D. Furthermore, we consider the case of a relatively blunt Gaussian disturbance in 2-D. In all cases, the agreement between the convolution results and simulations with a high-order Boussinesq model is outstanding. Finally, we make an attempt to extend the convolution methods to geophysical tsunami problems taking into account, e.g., uneven bottom effects. Unfortunately, refraction/diffraction effects cannot easily be incorporated, so instead we focus on the incorporation of linear shoaling and its effect on travel time and temporal evolution of the surface elevation. The procedure is tested on data from the 2011 Japan tsunami. Convolution results are likewise compared to model simulations based on the nonlinear shallow water equations and both are compared with field observations from 10 deep water DART buoys. The near-field results are generally satisfactory, while the far-field results leave much to be desired.

1. Introduction

Tsunamis generated by seismic activity in the deep ocean are typically transient wave trains propagating large distances over almost constant depth. During this propagation, nonlinearity is relatively small and the wave train can be assumed to be linear. The front of the wave train moves approximately with the linear shallow water celerity, while the leading wave is influenced by weak dispersion. Behind the leading wave, a tail with more dispersive waves will appear and dispersion will gradually become more and more important with the distance from the leading wave. The significance of the tail depends on the spatial gradients of the initial disturbance: Very sharp disturbances will immediately generate strong tails with highly dispersive waves, while blunt disturbances will produce only a single leading wave. During the propagation over large distances, however, transient waves will evolve under the accumulated influence of dispersion, leading to a gradual change of representative wave periods and a stronger and stronger dispersive tail.

Weak dispersion can typically be handled by any standard Boussinesq model and these are now being used for tsunami modeling on a regular basis [see e.g., *Løvholt et al.*, 2012; *Glimsdal et al.*, 2013; *Grilli et al.*, 2013]. It is, however, still common to use models based on the nondispersive nonlinear shallow water (NSW) equations [see e.g., *Tang et al.*, 2012; *Ren et al.*, 2013]. In principle, the NSW equations cannot correctly predict the temporal evolution of the transient waves, but it has to be admitted that these models have been relatively successful in simulating geophysical tsunamis.

In this work, we shall focus on transient linear dispersive water waves, induced by an initial localized disturbance and propagating over a constant depth. Our goal is to develop a fast, flexible, and accurate semianalytical model for the evolution of these waves and to incorporate full dispersion in this process. Fundamentally, this corresponds to the classical Cauchy-Poisson problem, which has been described by, e.g., *Lamb* [1932], *Wehausen and Laitone* [1960], and *LeBlond and Mysak* [1978]. First of all, the surface

elevation can be expressed by integral transforms relating the fluid motion at time t and position x to the prescribed initial disturbance. Second, these transforms can be approximated by asymptotic expansions valid for relatively large values of time and space from the disturbance. Classical solutions to this problem can be found in, e.g., *Kajiura* [1963], *Whitham* [1974], and *Newman* [1991]. These solutions typically describe the evolution of the leading wave near the wave front (in which case, weak dispersion can be assumed) or the trailing waves far behind the wave front, in which case, the method of stationary phase can be utilized. The classical solutions are nonuniform as they cannot describe the complete range of wave numbers present in the wave train.

Clarisse et al. [1995] were the first to develop *uniform* asymptotic solutions to the Cauchy-Poisson problem in both one and two dimensions, which implies that these solutions were uniformly valid for the complete interval of wave numbers (i.e., from weak dispersion to full dispersion). This was a remarkable achievement, but unfortunately their work has attracted very little attention. Today, 20 years later, their publication has obtained only six references according to Web of Science [e.g., *Kuznetsov*, 2006; *Ursell*, 2007; *Sekerzh-Zenkovich*, 2009; *Glimsdal et al*., 2007, 2013], none of which have actually utilized the findings of the original paper. Several reasons for this lack of attention could be suggested: First, the paper was very condensed and the method rather cumbersome. Second, no applications were presented leaving the full potential of the theory implied, rather than directly demonstrated. More recently, *Berry* [2005] presented a similar, but more elegant, derivation without being aware of the original work by *Clarisse et al*. [1995]. Berry provided a few applications but they were limited to idealized narrow Gaussian disturbances.

Our first objective in the present paper is to rederive and discuss the classical as well as the uniform asymptotic theory with the proper links to *Whitham* [1974], *Clarisse et al*. [1995], and *Berry* [2005]. In this connection, we start from the classical integral formulations in terms of Fourier and Hankel transforms and utilize a combination of the method of stationary phase, the method of uniform asymptotic approximations and various Airy integral formulations to obtain efficient but accurate impulse-response functions. Section 2 covers the case of an initial 1-D surface elevation, while section 3 covers the case of an initial 2-D radially symmetric surface elevation. Section 4 covers the variables of uniform approximations and discusses their variation behind, near, and beyond the front of the wave train.

Our second objective is to extend the uniform asymptotic theory beyond the achievements of Clarisse et al. and Berry by developing efficient convolution procedures in 1-D and 2-D in order to solve problems with general configurations of the initial disturbance. To this end, section 5 introduces efficient convolution techniques to be used for problems on a constant depth, while section 6 presents a number of test examples where the 1-D and 2-D approximations are applied and verified. This includes an initial 1-D rectangular disturbance, an initial 2-D square disturbance, and an initial 2-D Gaussian disturbance. The convolution solutions are compared with numerical results from models solving linear high-order Boussinesq equations [*Madsen et al*., 2002] as well as linear shallow water equations [*Ren et al*., 2013].

Our third objective is to investigate a possible extension of the asymptotic theories and their convolution methods to geophysical problems with uneven bottom. This has not been attempted previously in the literature, and success is by no means guaranteed. Ideally, this requires that shoaling, refraction, and diffraction are incorporated and furthermore it involves special effects related to the motion on a sphere. Unfortunately, diffraction and refraction effects are not readily incorporated in the present model, and we have chosen to focus on the incorporation of linear shoaling and its influence on the travel time of the leading wave. These effects are approximated by using linear shallow water theory, which is justified by the fact that natural tsunami sources often appear with relatively mild spatial gradients. Section 7 covers the extension to uneven bottom and a special convolution procedure suited for this purpose. As a test example, we focus on the 2011 Tohoku tsunami, and compare the convolution results with DART measurements and with numerical results obtained from solving the nonlinear shallow water equations [*Ren et al*., 2013].

2. The Response to an Initial 1-D Disturbance of the Free Surface

2.1. Introduction

We consider the classical problem of linear water waves generated by an initial disturbance of the free surface. A Cartesian coordinate system is adopted with the x axis located at the *still water level* (SWL) and with the z axis pointing vertically upward. Hence, the fluid domain is bounded by the horizontal sea bed at

$z = -h$ and by the free surface $z = \eta(x,t)$. Expressions will be derived in terms of nondimensional variables where horizontal (x) and vertical (z and η) distances are scaled with the water depth h, i.e.,

$$X \equiv \frac{x}{h}, \quad Z \equiv \frac{z}{h}, \quad \zeta \equiv \frac{\eta}{h}, \tag{1}$$

while time (t), cyclic frequency (ω), and the wave number (k) are nondimensionalized as

$$\tau \equiv t\sqrt{\frac{g}{h}}, \quad \Omega \equiv \omega\sqrt{\frac{h}{g}}, \quad \kappa \equiv kh, \tag{2}$$

where g is the acceleration of gravity. The linear dispersion relation for the wave propagation generally reads

$$\Omega^2 = \kappa \tanh \kappa,$$

with the associated relevant expression for $\Omega[\kappa]$ being

$$\Omega[\kappa] = \text{sign}[\kappa]\sqrt{\kappa \tanh \kappa}. \tag{3}$$

2.2. General Formulation Based on Fourier Integrals

The initial one-dimensional disturbance of the free surface is described by

$$\zeta[X,0] \equiv F[X], \text{ and } \zeta_\tau[X,0] = 0, \tag{4}$$

where $F[X]$ defines the arbitrary shape of this disturbance. As described by, e.g., *Whitham* [1974, section 13.5], the response to this disturbance is determined by

$$\zeta_1[X,\tau] = \int_{-\infty}^{\infty} \Gamma_1[\kappa](\exp[i(\kappa X - \Omega\tau)] + \exp[i(\kappa X + \Omega\tau)])d\kappa, \tag{5}$$

where $\Gamma_1[\kappa]$ is the Fourier transform of the initial condition, i.e.,

$$\Gamma_1[\kappa] = \frac{1}{4\pi}\int_{-\infty}^{\infty} F[X]\exp[-i\kappa X]dX. \tag{6}$$

For the special case of $F[X] = \delta[X]$, i.e., a 1-D Dirac delta-function disturbance, $\zeta_1[X,\tau]$ becomes the impulse-response function, while (6) yields

$$\Gamma_{1\delta}[\kappa] = \frac{1}{4\pi}. \tag{7}$$

In the following, we consider the asymptotic behavior of the solution for $\tau \to \infty$ and $X/\tau > 0$. This implies that the backward going waves can be ignored and (5) simplifies to

$$\zeta_2[X,\tau] = \int_{-\infty}^{\infty} \Gamma_1[\kappa]\exp[-i\tau\Phi]d\kappa, \tag{8}$$

where

$$\Phi \equiv \Omega[\kappa] - \kappa a, \quad \text{and} \quad a \equiv \frac{X}{\tau}. \tag{9}$$

Note that according to (1) and (2), we have that $a = x/(t\sqrt{gh})$. Hence, the front of the wave train, which moves with the nondispersive shallow water celerity, corresponds to $a \to 1$, while the dispersive tail of the transient wave corresponds to lower values of a.

2.3. The Method of Stationary Phase for Oscillating Integrals

The method of stationary phase was first discussed by *Stokes* [1850] and Lord Kelvin [see *Thomson*, 1887] and since then it has been used in many contexts in the literature. Good reviews of the method can be found in, e.g., *Whitham* [1974] and *Wong* [1989].

The objective is to approximate oscillating integrals of the type (8) for large values of τ. In this case, $\Gamma_1[\kappa]$ will typically be slowly varying, while the phase $\tau\Phi$ will oscillate rapidly with κ. This generally leads to cancelations in the integral unless there are points κ_i where the phase is stationary. These stationary points are defined by

$$\frac{d\Phi}{d\kappa}[\kappa_i]=0. \tag{10}$$

For the present case, the principal contribution to (8) comes from the two stationary points $\kappa=\pm\kappa_0$, where κ_0 satisfies

$$\frac{d\Phi}{d\kappa}=\Omega_\kappa[\kappa_0]-a=0, \quad \text{where} \quad \Omega_\kappa\equiv\frac{d\Omega}{d\kappa}. \tag{11}$$

We note that Ω_κ represents the local group velocity of the wave train.

Whitham [1974, section 11.3] and *Kajiura* [1963] used the method of stationary phase on (8) to derive the classical asymptotic approximation

$$\zeta_3[X,\tau]=2\Gamma_1[\kappa_0]\sqrt{\frac{2\pi}{-\tau\Omega_{\kappa,\kappa}}}\cos\left[-\tau\Phi[\kappa_0]+\frac{\pi}{4}\right], \tag{12}$$

where $\Omega_{\kappa,\kappa}$ denotes the second derivative of Ω with respect to κ.

2.4. The Weakly Dispersive Solution Valid Near the Front of the Wave Train

Whitham [1974, section 13.6] and *Kajiura* [1963] analyzed the conditions near the front of the wave train, where dispersion collapses and the waves become shallow water waves with $\kappa\to 0$. A brief summary of this derivation follows. First of all, a Taylor expansion about $\kappa=0$ of the linear dispersion relation leads to the KdV (Korteweg-de Vries) approximation

$$\Omega\simeq\kappa-\frac{1}{6}\kappa^3, \quad \Rightarrow \quad \Phi\simeq(1-a)\kappa-\frac{1}{6}\kappa^3, \tag{13}$$

and in this case (8) simplifies to

$$\zeta_4[X,\tau]=\Gamma_1[0]\int_{-\infty}^{\infty}\exp\left[i\kappa(X-\tau)+\frac{1}{6}i\kappa^3\tau\right]d\kappa. \tag{14}$$

At this point, it is useful to consider the definition of the Airy function

$$Ai[s]\equiv\frac{1}{\pi}\int_0^\infty\cos\left[sw+\frac{1}{3}w^3\right]dw=\frac{1}{2\pi}\int_{-\infty}^{\infty}\exp\left[i\left(sw+\frac{1}{3}w^3\right)\right]dw, \tag{15}$$

see e.g., *Vallée and Soares* [2004]. Hence, a comparison between (15) and (14) suggests the transformations

$$\frac{1}{3}w^3=\frac{1}{6}\tau\kappa^3 \quad \Rightarrow \quad \kappa=w\left(\frac{2}{\tau}\right)^{1/3}, \tag{16}$$

$$sw=\kappa(X-\tau) \quad \Rightarrow \quad s=(X-\tau)\left(\frac{2}{\tau}\right)^{1/3}=-(1-a)2^{1/3}\tau^{2/3}. \tag{17}$$

This implies that (14) can be expressed as

$$\zeta_4[X,\tau]=2\pi\Gamma_1[0]\left(\frac{2}{\tau}\right)^{1/3}Ai\left[-(1-a)2^{1/3}\tau^{2/3}\right]. \tag{18}$$

Figure 1 shows the spatial variation of the 1-D surface elevation as a function of $a=X/\tau$ at time $\tau=100$ for the special case of an initial delta-function disturbance. We note that ζ_3 given by (12) has a singularity near the front of the wave train where $a\to 1$ and $\Omega_{\kappa,\kappa}\to 0$. This problem is resolved by ζ_4 which describes the transition from the oscillatory motion behind the front ($a<1$) to the exponentially decaying motion

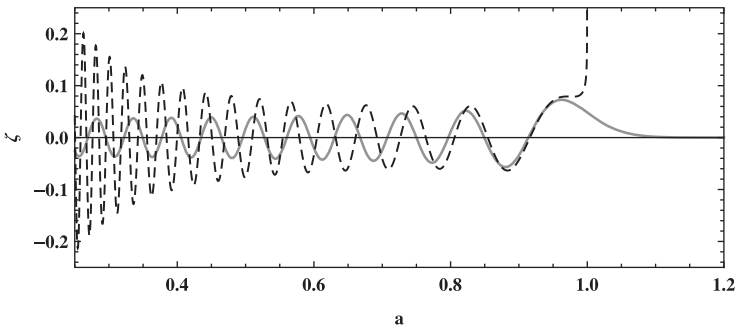

Figure 1. The 1-D impulse-response functions corresponding to a δ-function disturbance. Results obtained as a function of $a = X/\tau$ for $\tau = 100$. Full line, the weakly dispersive asymptotic approximation ζ_4 based on equation (18); dashed line, the classical asymptotic approximation ζ_3 based on equation (12).

beyond the front ($a > 1$). However, it is clear that the KdV dispersion relation imbedded in ζ_4 quickly becomes inadequate and the solution starts to deviate significantly from ζ_3 in phase as well as in amplitude for smaller values of a.

2.5. Uniform Asymptotic Approximations in 1-D

The main objective of the so-called *uniform* asymptotic approximations is to transform the integrand of oscillating integrals such as (8) into a simpler form allowing an analytical evaluation of the integral with the solution being uniformly valid for the complete interval of wave numbers (i.e., from weak dispersion to full dispersion). In contrast to the nonuniform procedures described in the previous section (and applied by e.g., *Kajiura* [1963] and *Whitham* [1974]), the uniform procedure retains full dispersion by mapping the variables of integration into a new set of variables while stretching the validity via the method of stationary phase. The general concept of uniform asymptotic transformations of oscillating integrals goes back to *Chester et al*. [1957], *Ursell* [1965], *Bleistein* [1966, 1967], *Child* [1975], and *Ursell* [1980]. More recent discussions of the technique can be found in *Wong* [1989], *Vallée and Soares* [2004], and *Ursell* [2007]. *Clarisse et al*. [1995] were the first to apply this method on the Cauchy-Poisson problem and their method for the 1-D problem will be summarized in the following.

In the frame work of Airy type solutions, Φ should be expressed as a cubic function. In this connection, *Clarisse et al*. [1995] used the form

$$\Phi[u] = \varepsilon u - \frac{1}{6}u^3, \tag{19}$$

while *Berry* [2005] used the form

$$\Phi[v] = -\sigma v - \frac{1}{3}v^3, \tag{20}$$

where u and v are new integration variables (replacing κ), while ε and σ are functions to be determined from matching conditions. Choosing (19) or (20) as the starting point is not important, and throughout this work we have chosen the (u, ε) formulation (19).

In the following, we shall now consider κ to be a function of u, and consequently (9) can be expressed as

$$\Phi[u] \equiv \Omega[\kappa[u]] - \kappa[u]a. \tag{21}$$

The matching of (19) and (21) now implicitly defines the new variable u.

On the basis of the transformation (19), we can replace (8) by

$$\zeta_5[X,\tau] = \int_{-\infty}^{\infty} \Gamma_1[\kappa[u]] G_1[u] \exp\left[i\tau\left(-\varepsilon u + \frac{1}{6}u^3\right)\right] du, \tag{22}$$

where

$$G_1[u] \equiv \frac{d\kappa}{du}. \tag{23}$$

The next step is to assume that Γ_1 and G_1 are slowly varying functions of u and to apply the method of stationary phase, by which the integral in (22) can be approximated by

$$\zeta_6[X,\tau]=\Gamma_1[\kappa_0]G_1[u_0]\int_{-\infty}^{\infty}\exp\left[i\tau\left(-\varepsilon u+\frac{1}{6}u^3\right)\right]du, \tag{24}$$

where u_0 defines the value of u at the first stationary point. A comparison with the definition of the Airy function (15) now suggests the transformations

$$\frac{1}{3}w^3=\frac{\tau}{6}u^3 \quad \Rightarrow \quad u=w\left(\frac{2}{\tau}\right)^{1/3}, \tag{25}$$

$$sw=-\tau\varepsilon u \quad \Rightarrow \quad s=-\varepsilon 2^{1/3}\tau^{2/3}. \tag{26}$$

This implies that (24) can be expressed as

$$\zeta_6[X,\tau]=2\pi\Gamma_1[\kappa_0]G_1[u_0]\left(\frac{2}{\tau}\right)^{1/3}Ai\left[-\varepsilon 2^{1/3}\tau^{2/3}\right], \tag{27}$$

where Γ_1 and G_1 are defined by (6) and (23), respectively. The determination of κ_0, u_0, ε, and $G_1[u_0]$ and the accuracy of (27) will be pursued in section 4.

3. The Response to an Initial 2-D Disturbance of the Free Surface

3.1. A Radially Symmetric Disturbance of the Free Surface

The linearized problem of an initial radially symmetric disturbance of the free surface was treated by, e.g., *Wehausen and Laitone* [1960], *Whitham* [1974], and *LeBlond and Mysak* [1978]. The initial disturbance is assumed to vary only with the radial distance $R \equiv r/h$ and have no angular dependence, i.e.,

$$\zeta[R,0] \equiv F[R], \text{ and } \zeta_\tau[R,0]=0. \tag{28}$$

As described by *Whitham* [1974, section 13.5], the surface elevation generated by this disturbance can be determined by

$$\zeta_{11}[R,\tau]=\int_0^{\infty}\Gamma_2[\kappa]J_0[\kappa R]\cos[\Omega\tau]\kappa d\kappa, \tag{29}$$

where Γ_2 is the Hankel transform defined by

$$\Gamma_2[\kappa]=\int_0^{\infty}F[R]J_0[\kappa R]RdR. \tag{30}$$

For the special case of a delta function located at the origin, $F[R]$ is defined by

$$F[R]=\frac{\delta[R]}{2\pi R}. \tag{31}$$

In this case, $\zeta_{11}[X,\tau]$ becomes the impulse-response function, and (30) leads to

$$\Gamma_{2\delta}[\kappa]=\frac{1}{2\pi}. \tag{32}$$

3.2. Uniform Asymptotic Approximations in 2-D

On the basis of the work by *Chester et al.* [1957], *Ursell* [1965], *Bleistein* [1966, 1967], and *Ursell* [1980], *Clarisse et al.* [1995] were the first to derive a 2-D uniform asymptotic approximation to (29) combined with (31). As a first step, they extended the integration from $-\infty$ to ∞, while replacing the Bessel function J_0 with the Hankel function $H_0^{(2)}$ of the second kind. Second, they replaced the Hankel function by its integral representation leading to the double integral

$$\zeta_{12}[R,\tau]=\frac{i2^{-3/2}}{2\pi^2}\int_{-\infty}^{\infty}\int_{-\infty}^{\infty}\kappa\left(1+\frac{1}{2}\sigma^2\right)^{-1/2}\exp[i\tau\Psi]d\kappa d\sigma,$$

with

$$\Psi \equiv \Omega[\kappa] - \kappa(1+\sigma^2)a, \quad \text{and} \quad a \equiv \frac{R}{\tau}.$$

Third, the integration variables (κ, σ) were replaced by the stretched variables (u, v) defined by the two relations

$$\varepsilon u - \frac{1}{6}u^3 = \Omega[\kappa] - \kappa a, \quad \text{and} \quad uv^2 = \kappa\sigma^2.$$

Fourth, these variables were replaced by a new set of stretched variables (ξ, λ) defined by

$$u = \alpha(\xi+\lambda), \quad \text{and} \quad v = \beta(\xi-\lambda).$$

With these transformations, the method of stationary phase resulted in four saddle points for ($\xi_0^{\pm}$, $\lambda_0^{\pm}$) and after cumbersome algebraic manipulations the surface elevation was finally expressed in terms of the product of the Airy function and its derivative.

More recently, *Berry* [2005] considered the same problem, apparently being unaware of the original work by *Clarisse et al.* [1995]. However, Berry pursued a much more direct and straight forward path, which we summarize in the following. First of all, the Bessel function J_0 is expressed by its integral definition

$$J_0[\kappa R] \equiv \frac{1}{2\pi}\int_0^{2\pi} \exp[i\kappa R\cos\theta]d\theta. \tag{33}$$

Second, the method of stationary phase is applied to (33) leading to the two stationary points $\theta_1 = 0$ and $\theta_2 = \pi$. Now a Taylor expansion about each of these points leads to

$$\cos\theta \simeq 1 - \frac{1}{2}\theta^2, \qquad \text{for } \theta \simeq \theta_1,$$
$$\cos\theta \simeq -1 + \frac{1}{2}(\theta-\pi)^2, \quad \text{for } \theta \simeq \theta_2,$$

by which the integration in (33) can be analytically executed near each stationary point. This leads to

$$\begin{aligned} J_0[\kappa R] &\simeq \frac{1}{2\pi}\left(\sqrt{\frac{\pi}{\kappa R}}(1-i)\exp[i\kappa R] + \sqrt{\frac{\pi}{\kappa R}}(1+i)\exp[-i\kappa R]\right) \\ &= \sqrt{\frac{2}{\pi\kappa R}}\cos\left[\kappa R - \frac{\pi}{4}\right]. \end{aligned} \tag{34}$$

We note that (34) is the classical asymptotic approximation for J_0 valid for large values of κR.

Next, (34) is inserted in (29) and as a result the integrand contains two terms, representing waves propagating away from and toward the source, respectively. The latter is ignored by which we obtain the following asymptotic approximation to (29)

$$\zeta_{13}[R,\tau] = \int_0^{\infty} \frac{\Gamma_2[\kappa]\kappa^{1/2}}{(2\pi R)^{1/2}}\cos\left[\tau\Phi + \frac{\pi}{4}\right]d\kappa, \tag{35}$$

where

$$\Phi[\kappa] \equiv \Omega[\kappa] - \kappa a, \quad a \equiv \frac{R}{\tau}. \tag{36}$$

The next step is to introduce the uniform transformation of variables exactly as in 1-D, i.e., κ is replaced by u defined by (19). In this process, the following connection is utilized

$$\kappa^{1/2}d\kappa = G_2 u^{1/2}du, \tag{37}$$

where

$$G_2 \equiv \frac{d\kappa}{du}\sqrt{\frac{\kappa}{u}}. \tag{38}$$

The functions G_2 and Γ_2 are assumed to be slowly varying with u and are therefore estimated by their values at the stationary phase points $u = \pm u_0$. On this basis, the integral (35) transforms into

$$\zeta_{14}[R,\tau]=\frac{\Gamma_2[u_0]G_2[u_0]}{(2\pi R)^{1/2}}\int_0^\infty \cos\left[\tau\left(\varepsilon u-\frac{1}{6}u^3\right)+\frac{\pi}{4}\right]u^{1/2}du. \tag{39}$$

It turns out that this integral can be expressed in terms of Airy functions. *Berry* [2005] provided the result in his equation ((5).5), but omitted the derivation, which is given here, as we do not find it completely trivial. The starting point is to consider the following integral definition of the product of the Airy function and its derivative

$$Ai[s]Ai'[s]\equiv\left(\frac{1}{2\pi}\right)^2\int_{-\infty}^{\infty}\int_{-\infty}^{\infty} iv\exp\left[i\left((v+w)s+\frac{1}{3}\left(v^3+w^3\right)\right)\right]dvdw. \tag{40}$$

Next, we introduce a coordinate transformation from (v, w) variables to (ξ, λ) variables defined by

$$w=\beta(\xi+\lambda),\quad \text{and}\quad v=\beta(\xi-\lambda). \tag{41}$$

The absolute value of the corresponding Jacobian determinant is $2\beta^2$. With this coordinate transformation, it is now possible to analytically integrate the λ-integral and as a result (40) simplifies to

$$Ai[s]Ai'[s]=-\frac{1}{2^{1/2}\pi^{3/2}}\int_0^\infty \cos\left[-2\xi\beta s-\frac{2}{3}\xi^3\beta^3+\frac{\pi}{4}\right]\beta^{3/2}\xi^{1/2}d\xi. \tag{42}$$

The matching of (42) and (39) now yields

$$u=\frac{2}{\tau^{1/2}}\xi,\quad s=-\frac{\varepsilon\tau^{2/3}}{2^{1/3}},\quad \beta=\frac{2^{1/3}}{\tau^{1/6}},$$

and as a result the asymptotic surface elevation can be determined by

$$\zeta_{15}[R,\tau]=-\frac{2\pi\Gamma_2[\kappa_0]G_2[u_0]}{\sqrt{R\tau}}Ai\left[-\varepsilon 2^{-1/3}\tau^{2/3}\right]Ai'[-\varepsilon 2^{-1/3}\tau^{2/3}], \tag{43}$$

where Γ_2 and G_2 are defined by (30) and (38), respectively. The determination of κ_0, u_0, ε, $G_1[u_0]$, and $G_2[u_0]$ will be pursued in section 4.

4. The Governing Parameters in the Uniform Asymptotic Approximations

Before we can utilize the uniform asymptotic approximations given in (27) for 1-D and (43) for 2-D, we need to determine κ_0, u_0, ε, $G_1[u_0]$, and $G_2[u_0]$ at the stationary points. The following derivation is split into three parts: First, we concentrate on conditions behind the wave front, i.e., for $0<a<1$. Second, we focus on conditions ahead of the front, i.e., for $a>1$. Third, we present Taylor expansions for $a\to 1$. These expressions will bridge the formulations behind and ahead of the front, and in addition they will provide practical approximations to the general expressions.

4.1. Solutions for $0<a<1$

In order to determine $\kappa=\kappa_0$, we first differentiate the dispersion relation (3) with respect to κ and obtain

$$\Omega_\kappa=\text{sign}[\kappa]\left(\frac{\kappa\,\text{sech}^2\kappa+\tanh\kappa}{2\sqrt{\kappa\tanh\kappa}}\right). \tag{44}$$

This is an even function of κ, i.e., $\Omega_\kappa[-\kappa]=\Omega_\kappa[\kappa]$ and for this reason (11) will be satisfied by κ_0 as well as by $-\kappa_0$. We assume that $\kappa_0>0$, and insert (44) in (11), which leads to the condition

$$\frac{\kappa_0\,\text{sech}^2\kappa_0+\tanh\kappa_0}{2\sqrt{\kappa_0\tanh\kappa_0}}=a,\quad \text{for}\ \kappa_0>0. \tag{45}$$

For $0<a<1$, (45) will provide real number solutions for κ_0, which will obviously be a function of a.

Next, let us determine the value of $u=u_0$ at the first stationary point $\kappa=\kappa_0$. First, we differentiate (19) with respect to u to obtain

$$\frac{d\Phi}{du}=\varepsilon-\frac{1}{2}u^2. \tag{46}$$

Second, we differentiate (21) with respect to u to obtain

$$\frac{d\Phi}{du}=\frac{d\kappa}{du}(\Omega_\kappa-a). \tag{47}$$

According to (11), it is clear that (47) will be zero at the first stationary point, and consequently (46) also needs to be zero. This leads to the matching condition

$$\varepsilon=\frac{1}{2}u_0^2. \tag{48}$$

Third, (19) and (21) obviously need to match for all values of u and therefore also at the first stationary point $u=u_0$. According to (48), this leads to

$$\Phi[u_0]=\frac{1}{3}u_0^3, \quad \text{and } \Phi[u_0]=\Omega[\kappa_0]-\kappa_0 a, \tag{49}$$

by which we obtain

$$u_0=3^{1/3}(\Omega[\kappa_0]-\kappa_0 a)^{1/3}, \tag{50}$$

$$\varepsilon=\frac{1}{2}3^{2/3}(\Omega[\kappa_0]-\kappa_0 a)^{2/3}. \tag{51}$$

With κ_0 being a function of a, we note that also u_0 and ε are functions of a.

Fourth, we need to evaluate $G_1[u]$ defined by (23). By matching (46) and (47), we obtain the general expression

$$G_1[u]\equiv\frac{d\kappa}{du}=\left(\frac{\varepsilon-\frac{1}{2}u^2}{\Omega_\kappa-a}\right). \tag{52}$$

Toward the first stationary point, the numerator and the denominator of (52) go to zero. Consequently, we need to Taylor-expand the numerator as well as the denominator with respect to u in the vicinity of u_0 until we get nonzero contributions. Thus, by applying L'Hôspital's rule on (52) we obtain

$$\Omega_{\kappa,\kappa}\left(\frac{d\kappa}{du}\right)^2=-u, \quad \text{for } u=u_0,$$

which leads to the result

$$G_1[u_0]\equiv\frac{d\kappa}{du}[u_0]=\sqrt{\frac{u_0}{-\Omega_{\kappa,\kappa}[\kappa_0]}}. \tag{53}$$

Note that u_0 is given by (50), while $\Omega_{\kappa,\kappa}$ can be determined by differentiating (44) with the result

$$\Omega_{\kappa,\kappa}[\kappa]=\text{sign}[\kappa]\left(\frac{-1+3\kappa^2\text{sech}^4\kappa+\text{sech}^2\kappa(1-4\kappa^2+2\kappa\tanh\kappa)}{4(\kappa\tanh\kappa)^{3/2}}\right). \tag{54}$$

We note that $\Omega_{\kappa,\kappa}$ is an odd function of κ, i.e., that $\Omega_{\kappa,\kappa}[-\kappa]=-\Omega_{\kappa,\kappa}[\kappa]$.

Finally, we need to evaluate $G_2[u]$ defined by (38). By inserting (53) we obtain

$$G_2[u_0]\equiv\sqrt{\frac{\kappa_0}{u_0}}\frac{d\kappa}{du}[u_0]=\sqrt{\frac{\kappa_0}{-\Omega_{\kappa,\kappa}[\kappa_0]}}. \tag{55}$$

4.2. Taylor Expansions for $a\to 1$

Near the front of the wave train, we have that $a\to 1$ and $\kappa_0\to 0$, hence we introduce the small parameter $\mu\equiv 1-a$. To obtain a Taylor expansion of κ_0 in terms of μ, we first expand (45) in terms of κ_0^2, then use successive approximations to invert this series as κ_0^2 in terms of μ and finally we expand the square root of this series to obtain

$$\kappa_0=\sqrt{2\mu}\left(1+\frac{19}{36}\mu+\frac{1207}{2592}\mu^2+\frac{2588183}{5443200}\mu^3+\ldots.\right) \quad \text{for } \mu \to 0. \tag{56}$$

Next, we Taylor-expand u_0 and ε from (50) and (51) with respect to κ_0 and substitute (56) into the result. This leads to

$$u_0=\sqrt{2\mu}\left(1+\frac{19}{180}\mu+\frac{25121}{453600}\mu^2+\frac{1996219}{48988800}\mu^3+\ldots.\right) \quad \text{for } \mu \to 0, \tag{57}$$

$$\varepsilon=\mu\left(1+\frac{19}{90}\mu+\frac{64}{525}\mu^2+\frac{178328}{1913625}\mu^3+\ldots.\right) \quad \text{for } \mu \to 0. \tag{58}$$

Finally, we Taylor-expand $G_1[u_0]$ and $G_2[u_0]$ with respect to κ_0 by inserting (50) and (54) into (53) and (55). By substituting (56) into the result, we obtain

$$G_1[u_0] \to \left(1+\frac{38}{45}\mu+\frac{521}{567}\mu^2+\frac{411574}{382725}\mu^3+\ldots.\right) \quad \text{for } \mu \to 0. \tag{59}$$

$$G_2[u_0] \to \left(1+\frac{19}{18}\mu+\frac{815}{648}\mu^2+\frac{1059679}{680400}\mu^3+\ldots.\right), \quad \text{for} \mu \to 0. \tag{60}$$

4.3. Solutions for $a > 1$

In order to extend the formulation to the region ahead of the front, we first need to find solutions to

$$\Omega_\kappa[\kappa_0]=a, \quad \text{for } a > 1. \tag{61}$$

This requires that κ_0 falls on the imaginary axis, hence we introduce

$$\kappa_0=i\tilde{\kappa}_0, \text{ and } u_0 = i\tilde{u}_0, \tag{62}$$

where the *tilde* indicates real number variables. According to (3), (44), and (54), this leads to

$$\Omega[i\tilde{\kappa}_0]=i\sqrt{\tilde{\kappa}_0\tan\tilde{\kappa}_0}, \tag{63}$$

$$\Omega_\kappa[i\tilde{\kappa}_0]=\frac{\tilde{\kappa}_0\sec^2\tilde{\kappa}_0+\tan\tilde{\kappa}_0}{2\sqrt{\tilde{\kappa}_0\tan\tilde{\kappa}_0}}, \tag{64}$$

$$\Omega_{\kappa,\kappa}[i\tilde{\kappa}_0]=i\left(\frac{-1-3\tilde{\kappa}_0^2\sec^4\tilde{\kappa}_0+\sec^2\tilde{\kappa}_0\left(1+4\tilde{\kappa}_0^2-2\tilde{\kappa}_0\tan\tilde{\kappa}_0\right)}{4\left(\tilde{\kappa}_0\tan\tilde{\kappa}_0\right)^{3/2}}\right). \tag{65}$$

This implies that $\tilde{\kappa}_0$ is found as the solution to

$$\frac{\tilde{\kappa}_0\sec^2\tilde{\kappa}_0+\tan\tilde{\kappa}_0}{2\sqrt{\tilde{\kappa}_0\tan\tilde{\kappa}_0}}=a, \quad \text{for } a > 1. \tag{66}$$

Next, we determine $\tilde{u}_0$ and ε by inserting (62) and (63) into (49) and (48). This leads to

$$\tilde{u}_0=3^{1/3}\left(\tilde{\kappa}_0 a-\sqrt{\tilde{\kappa}_0\tan\tilde{\kappa}_0}\right)^{1/3}, \quad \text{for } a > 1, \tag{67}$$

$$\varepsilon=-\frac{1}{2}3^{2/3}\left(\tilde{\kappa}_0 a-\sqrt{\tilde{\kappa}_0\tan\tilde{\kappa}_0}\right)^{2/3}, \quad \text{for } a > 1. \tag{68}$$

Note that in contrast to κ_0 and u_0, the continuation of ε from behind the front to ahead of the front actually takes place in the real domain.

Finally, we insert (62) and (65) into (53) and (55) and obtain

$$G_1[u_0]=\sqrt{\frac{\tilde{u}_0}{-\tilde{\Omega}_{\kappa,\kappa}[\tilde{\kappa}_0]}}, \quad \text{and} \quad G_2[u_0]=\sqrt{\frac{\tilde{\kappa}_0}{-\tilde{\Omega}_{\kappa,\kappa}[\tilde{\kappa}_0]}}, \quad \text{for } a > 1. \tag{69}$$

We note that G_1 and G_2 fall on the real axis also for $a > 1$.

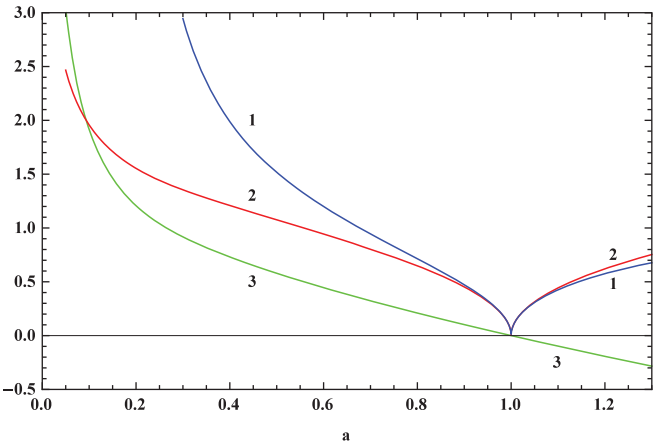

Figure 2. The variation of κ_0 (1), u_0 (2), and ε (3) as a function of $a = X/\tau$.

4.4. The Resulting Surface Elevations in 1-D and 2-D

Having determined $G_1[u_0]$ and $G_2[u_0]$, we can now insert (53) and (55) into (27) and (43) to obtain the 1-D surface elevation

$$\zeta_7[X,\tau] = 2\pi\Gamma_1[\kappa_0]\sqrt{\frac{u_0}{-\Omega_{\kappa,\kappa}[\kappa_0]}}\left(\frac{2}{\tau}\right)^{1/3} Ai\left[-\varepsilon 2^{1/3}\tau^{2/3}\right], \tag{70}$$

and the 2-D surface elevation

$$\zeta_{16}[R,\tau] = -\frac{2\pi\Gamma_2[\kappa_0]}{\sqrt{R\tau}}\sqrt{\frac{\kappa_0}{-\Omega_{\kappa,\kappa}[\kappa_0]}} Ai\left[-\varepsilon 2^{-1/3}\tau^{2/3}\right] Ai'\left[-\varepsilon 2^{-1/3}\tau^{2/3}\right]. \tag{71}$$

We note that Γ_1 and Γ_2 are defined by (6) and (30), while κ_0, u_0, and ε are functions of a as defined by (45), (50), and (51). Furthermore, we note that $a \equiv X/\tau$ in 1-D and $a \equiv R/\tau$ in 2-D.

It should be emphasized that (70) and (71) can be shown to agree with *Berry* [2005, equations (4.3) and (5.6)]. *Clarisse et al.* [1995] focused from the very beginning on the response to delta-function disturbances, so their expressions can in principle be retrieved by using $\Gamma_{1\delta} = 1/(4\pi)$ and $\Gamma_{2\delta} = 1/(2\pi)$. There is, however, generally a factor 2π difference between the results of Clarisse et al. and (70) and (71). Furthermore, for some reason they did not apply (53) for G_1 but promoted the approximation $G_1 \simeq \varepsilon/(1-a)$.

Figure 2 shows the variation of κ_0, u_0, and ε as a function of a according to (45), (50), and (51). The kinks at $a = 1$ for the continuations of κ_0 and u_0 are typical for functions jumping from the real axis to the imaginary axis at this location.

Figure 3 shows the variation of $G_1[u_0]$ as a function of a according to (53). The polynomial approximation (59) is accurate within $0.5 < a \leq 1$. The figure also includes the approximation $G_1 \simeq \varepsilon/(1-a)$ suggested by *Clarisse et al.* [1995], but this is seen to be very inaccurate and cannot be recommended.

Figure 4 shows the spatial variation of the 1-D surface elevation as a function of $a = X/\tau$ at time $\tau = 100$ for the special case of an initial delta-function disturbance. We compare ζ_3 given by (12) and ζ_7 given by (70) and notice a remarkable agreement for $a < 0.95$. This clearly demonstrates that the uniform transformation is able to capture the full dispersion rather than just the KdV dispersion which was shown in Figure 1.

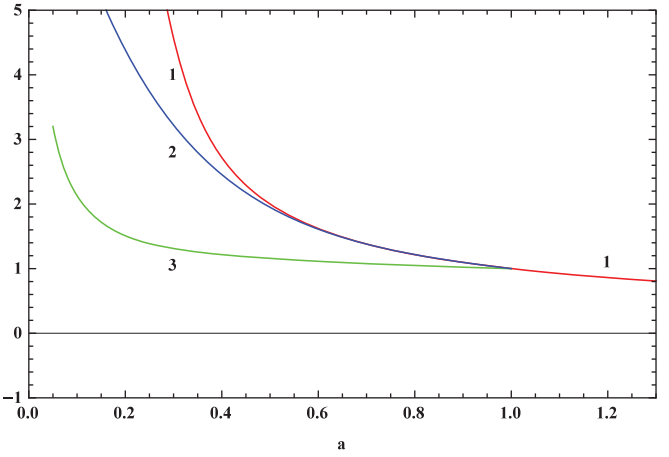

Figure 3. The variation of $G_1[u_0]$ as a function of $a = X/\tau$. (1) Full solution according to equation (53) including extension into the complex domain according to equation (69); (2) Taylor approximation according to equation (59); and (3) the approximation proposed by *Clarisse et al.* [1995], i.e., $\varepsilon/(1-a)$.

5. Convolution in One and Two Dimensions

For simple initial disturbances such as Gaussian distributions, it is straight forward to determine $\Gamma_1[\kappa]$ and $\Gamma_2[\kappa]$ analytically on the basis of (6) and (30). In this case, the resulting surface elevation can be determined either by direct numerical integration of (8) and (29) or from the asymptotic

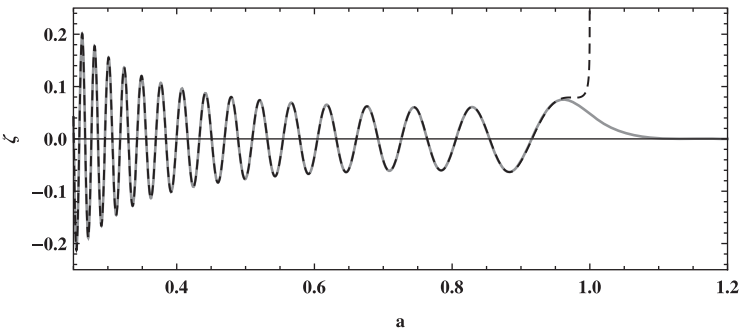

Figure 4. The 1-D impulse-response functions corresponding to a δ-function disturbance. Results obtained as a function of $a = X/\tau$ for $\tau = 100$. Full line, the uniform (fully dispersive) asymptotic approximation ζ_7 based on equation (70); dashed line, the classical asymptotic approximation ζ_3 based on equation (12).

approximations (70) and (71). However, in more general cases, $\Gamma_1[\kappa]$ and $\Gamma_2[\kappa]$ cannot be determined analytically, and here we use the delta-function formulations combined with convolution integrals as described in the following.

5.1. Convolution in 1-D

To solve the 1-D problem of an initial condition given as $\zeta[X,0]=F[X]$, we utilize convolution integration based on the impulse-response function ζ_7 with the delta function located at the origin. This is defined by (70) combined with $\Gamma_{1\delta}=1/(4\pi)$. Typically, we can assume that $F[X] \neq 0$ for $X_{\min} \leq X \leq X_{\max}$ and identical to zero outside this interval. In this case, the convolution integral reads

$$\tilde{\zeta}[X_0,\ \tau]=\int_{X_{\min}}^{X_{\max}} F[X]\zeta_7[X_0-X,\ \tau]dX, \tag{72}$$

where X_0 is the observation coordinate, X is the integration coordinate covering the source region, and ζ_7 is given by (70). In order to speed up the procedure, we first create interpolation functions for $\varepsilon[a]$ and $G_1[u_0]$ covering the interval $0 < a < 2.5$, and second we evaluate the integral numerically as

$$\tilde{\zeta}[X_0,\ \tau]=\Delta X \sum_{X=X_{\min}}^{X_{\max}} F[X]\zeta_7[X_0-X,\ \tau], \tag{73}$$

where the increments are chosen as

$$\Delta X=\frac{X_{\max}-X_{\min}}{n_x-1}, \tag{74}$$

with n_x being the number of grid points.

5.2. Convolution in 2-D

To solve the 2-D problem of an initial condition given as $\zeta[X,Y,0]=F[X,Y]$, we utilize convolution integration based on the radially symmetric impulse-response function ζ_{16} with the delta function located at the origin. This is defined by (71) combined with $\Gamma_{2\delta}=1/(2\pi)$. The convolution formulation in rectangular coordinates reads

$$\tilde{\zeta}[X_0,\ Y_0,\ \tau]=\int_{Y_{\min}}^{Y_{\max}}\int_{X_{\min}}^{X_{\max}} F[X,\ Y]\ \zeta_{16}[R[X,\ Y,\ X_0,Y_0],\ \tau]dXdY, \tag{75}$$

where (X_0, Y_0) defines the observation point, (X, Y) defines the integration coordinate covering the source region, and R defines the distance between these points given by

$$R[X,\ Y,\ X_0,\ Y_0]=\sqrt{(X-X_0)^2+(Y-Y_0)^2}. \tag{76}$$

In practise, we evaluate the double integral numerically by the double summation

$$\tilde{\zeta}[X_0,\ Y_0,\ \tau]=\Delta X\Delta Y \sum_{X=X_{\min}}^{X_{\max}}\sum_{Y=Y_{\min}}^{Y_{\max}} F[X,\ Y]\ \zeta_{16}[R[X,\ Y,\ X_0,\ Y_0],\ \tau]. \tag{77}$$

The case is illustrated by Figure 5, where the observation point is located at O and the initial disturbance is located within the area with corner points A, B, C, and D centered at the origin of the rectangular coordinate

system (X, Y). These corner points define the values of $X_{\min}$, $X_{\max}$, $Y_{\min}$, and $Y_{\max}$, while the discrete increments are given by

$$\Delta X = \frac{X_{\max} - X_{\min}}{n_x - 1}, \quad \Delta Y = \frac{Y_{\max} - Y_{\min}}{n_y - 1}, \tag{78}$$

with, e.g., n_x and n_y being the number of grid points.

One way to speed up the process is to introduce a local polar coordinate system (s, θ) centered at the observation point O, i.e., at (X_0, Y_0). This leads to the coordinate transformation

$$\begin{aligned} X &\equiv X_0 - s\cos\theta, \\ Y &\equiv Y_0 - s\sin\theta, \end{aligned} \tag{79}$$

where s denotes the distance from (X_0, Y_0) to (X, Y). Now the convolution summation can take place in discrete s and θ increments, e.g., within the sector of the annulus confined by the points E, F, G, and H (see Figure 5). With ζ_{16} being radially symmetric, i.e., independent of the angle θ this leads to the simplification

$$\tilde{\zeta}[X_0,\ Y_0,\ \tau] = \Delta s \Delta\theta \sum_{s=R_{\min}}^{R_{\max}} \left(\sum_{\theta=\theta_{\min}}^{\theta_{\max}} F[X_0 - s\cos\theta,\ Y_0 - s\sin\theta] \right) s\zeta_{16}[s,\tau], \tag{80}$$

where

$$\Delta s = \frac{R_{\max} - R_{\min}}{n_R - 1}, \quad \Delta\theta = \frac{\theta_{\max} - \theta_{\min}}{n_\theta - 1}. \tag{81}$$

The limits of $R_{\max}$, $R_{\min}$, $\theta_{\max}$, and $\theta_{\min}$ are readily determined from the location of the E, F, G, and H points in Figure 5.

An alternative and even faster procedure is outlined in the following: first, the distance R between the observation point and each of the discrete integration points within the domain of the initial disturbance is determined. Now we have a map of associated {R, F} values representing distance and source values at all discrete integration points. Typically, a specific value of R will occur at several grid points and therefore be associated with several values of F. This is illustrated in Figure 6 (top), which shows the discrete values of F as a function of the associated values of R for the case of a Gaussian disturbance. The next step is to cover the interval from $R_{\min}$ to $R_{\max}$ by increments of Δs (as defined by (81)) and to sum up all F-values falling within these discrete Δs-bins. This leads to the accumulated source function

$$E[s] = \sum F[s], \tag{82}$$

which is illustrated in Figure 6 (bottom) for the case of a Gaussian disturbance. With this information at hand, we can simplify the double summation (77) to the single summation

$$\tilde{\zeta}[X_0,\ Y_0,\ \tau] = \Delta X \Delta Y \sum_{s=R_{\min}}^{R_{\max}} E[s]\ \zeta_{16}[s,\ \tau]. \tag{83}$$

This procedure is extremely fast and provides the resulting time series in a few seconds.

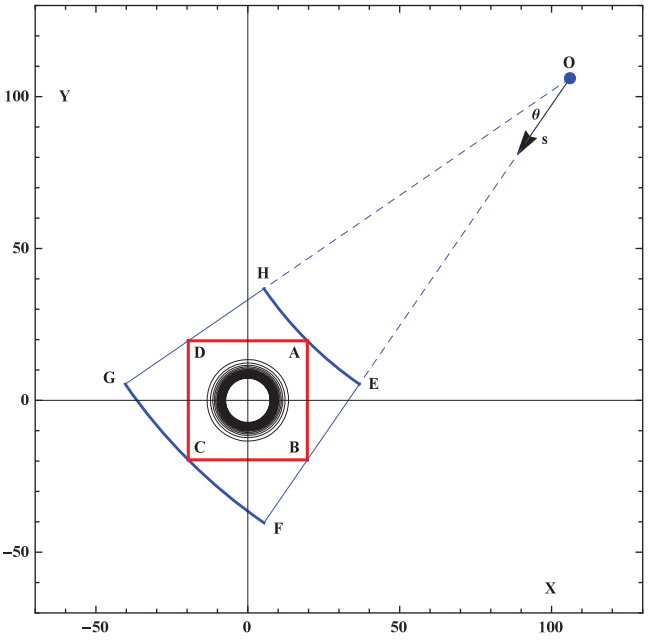

Figure 5. Sketch illustrating the convolution procedure in 2-D. As an example, an initial Gaussian disturbance is contained in the square with corner points A, B, C, and D. The integration points are expressed in local polar coordinates with the observation point O as origin. Actual convolution integration takes place within the sector of the annulus (confined by the points E, F, G, and H).

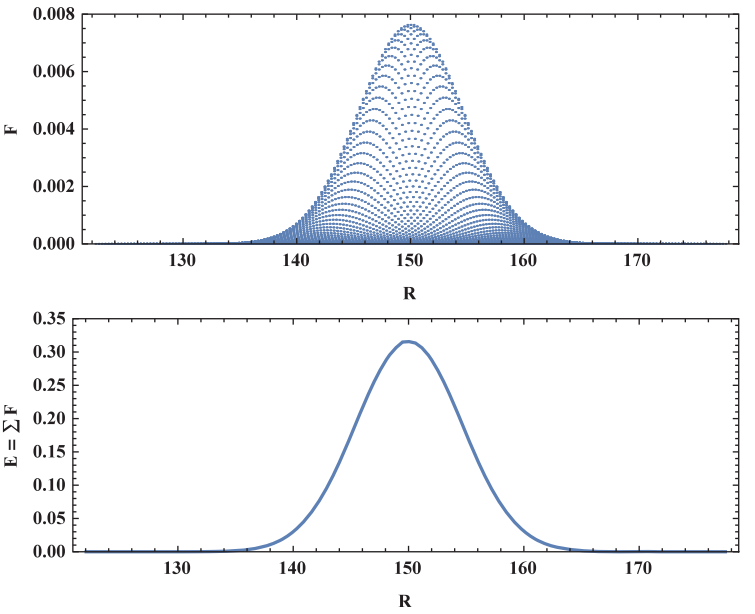

Figure 6. The discrete values of an initial Gaussian disturbance F shown as a function of the associated distance R from the selected observation point to each of the integration points. (top) F as a function of R; (bottom) sum of F within discrete R bins based on equation (82).

6. Applications on a Constant Depth

6.1. The Case of an Initial 1-D Rectangular Disturbance

We first consider a 1-D sharp-edged rectangular disturbance described by $F[X] = F_0$ within $x_{min} \le x \le x_{max}$. This will generate a transient wave with a highly dispersive tail, and as reference, we apply a linear high-order Boussinesq model [see e.g., *Madsen et al.*, 2002; *Fuhrman and Bingham*, 2004], which incorporates accurate dispersion properties up to dimensionless wave numbers of $\kappa = 25$. A similar test case was studied by *Madsen and Schäffer* [2010, section 7.2]. In dimensional variables, we use $h_0 = 4000$ m, $x_{max} = -150$ km, $x_{min} = -400$ km and consider the observation point $x_0 = 12{,}000$ km. This corresponds to the nondimensional parameters $X_{max} = -37.5$, $X_{min} = -100$, and $X_0 = 3000$. It is emphasized that Madsen and Schäffer used an initial amplitude of 3 m, but this was combined with a reflecting wall at the input boundary so in the present formulation this corresponds to $F_0 = 6/4000 = 0.0015$. The numerical Boussinesq solution is computed using a fixed grid of $dx = 400$ m, a time step of $dt = 2$ s, and a total of 40,001 grid points and 40,001 time steps. The convolution solution is obtained by using (73) and (74) with $n_x = 200$.

Figures 7a and 7b show a comparison of the linear Boussinesq solution (dashed line) and the convolution solutions (full gray lines). The top figure shows the performance of the nonuniform weakly dispersive formulation $\tilde{\zeta}_4$ (given by (18)). This is fairly accurate for the first 60 min of the time series, but beyond this point discrepancies in phase and amplitude show up. The bottom figure shows the performance of the fully dispersive uniform formulation $\tilde{\zeta}_7$ (given by (70)). This is obviously more accurate than the nonuniform formulation. The differences between the two convolution solutions increase significantly when we continue the time series in Figures 8a and 8b, now covering from 1150 to 1300 min. According to the top figure, the nonuniform formulation is now completely off in amplitude and phase, while

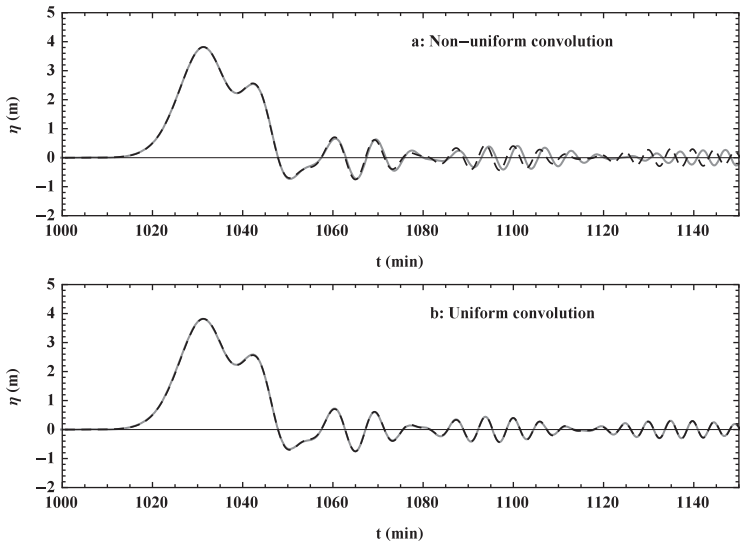

Figure 7. First part of the time series of the surface elevation due to a monopole source. Numerical simulation with linear high-order Boussinesq model is shown as the dashed lines. The convolution solution based on the nonuniform KdV approximation ζ_4 is shown as the full line in the top figure. The convolution solution based on the uniform approximation ζ_7 is shown as the full line in the bottom figure.

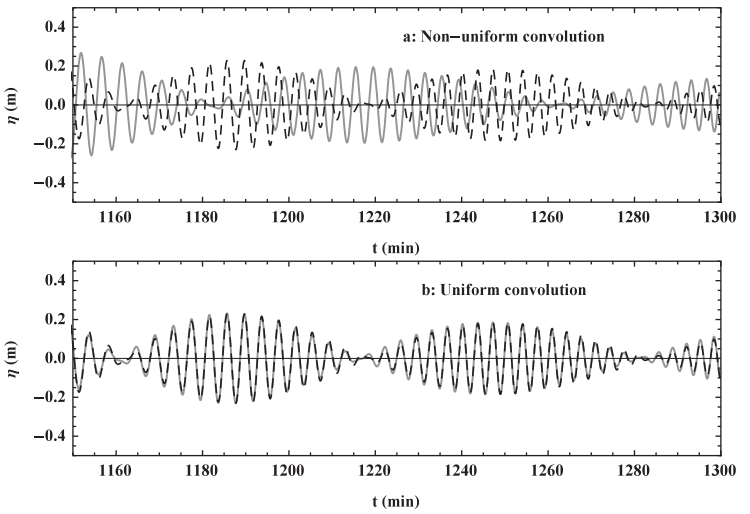

Figure 8. Second part of the time series of the surface elevation due to a monopole source. Description as in Figure 7.

the uniform formulation, shown in the bottom figure, is in very good agreement with the Boussinesq simulation. This confirms the accuracy of the uniform asymptotic approximation versus the conventional KdV approximation.

6.2. The Case of an Initial 2-D Square Disturbance

We continue with a square sharp-edged disturbance in 2-D, which again is expected to generate a transient wave with a highly dispersive tail. The initial disturbance is shown in Figure 5, where the points *A*, *B*, *C*, and *D* are located at (b_1, b_1), $(b_1, -b_1)$, $(-b_1, -b_1)$, and $(-b_1, b_1)$, with $b_1 = 32$ km and where the initial amplitude within this area is $a_1 = 16$ m. The volume of this initial disturbance is therefore $4a_1b_1^2$. The water depth is constant and equal to $h = 4.0$ km. The location of the observation points are generally specified by

$$x_0 = r_0 \cos\varphi_0, \quad y_0 = r_0 \sin\varphi_0. \tag{84}$$

Again, we use the linear high-order Boussinesq model as reference, but this time we also include computations based on the nondispersive linear shallow water model [*Ren et al.*, 2013] in order to illustrate the influence of dispersion. Both models are set up to cover the first quadrant of the problem using 2000 by 2000 grid points with grid size $dx = dy = 1.0$ km and 3000 time steps with step size $dt = 5.0$ s. A perspective snapshot of the computed surface elevation is shown in Figure 9.

The convolution method covers the initial disturbance area with $n_x = n_y = 100$ grid points in rectangular coordinates and $n_R = n_\theta = 100$ grid points in polar coordinates. Double summation of (77) in rectangular coordinates takes approximately 400 s, while double summation of (80) in polar coordinates takes about 30 s. Finally, the single summation (83) takes about 4 s. Results obtained by the three different convolution methods are virtually identical and consequently only the single summation results are shown.

Figures 10a–10d show the computed temporal variation of the surface elevation at four locations defined by $r_0 = 600$ km and $\varphi_0 = 0, \pi/16, \pi/8$, and $\pi/4$, respectively. We notice that the dispersive tail of the wave train is much stronger for small angles in contrast to the case of $\varphi_0 = \pi/4$ where it is almost absent. The convolution solution based on (83) is shown as gray lines, the linear Boussinesq results as black lines and the linear shallow water results as dashed lines. Generally, there is very little difference between the convolution solution and the Boussinesq results. We notice that the nondispersive shallow water model can only represent the leading wave, and this is typically overestimated if the tail is present in the

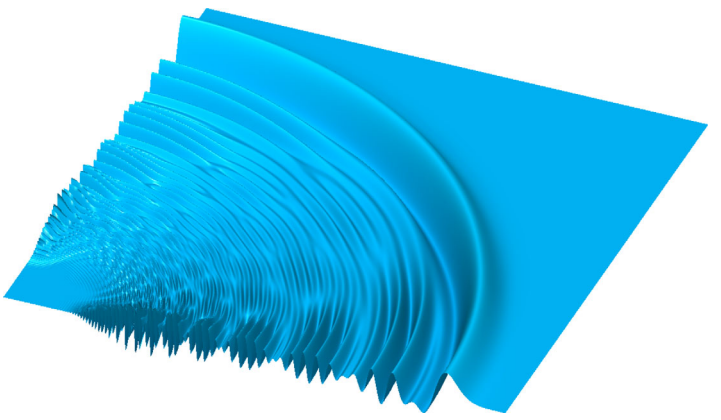

Figure 9. Snapshot of the surface elevation computed by the Boussinesq model for an initial square disturbance released at the lower left corner. Model dimensions are 2000 by 2000 grid points with a grid size of 1 km and a water depth of 4 km.

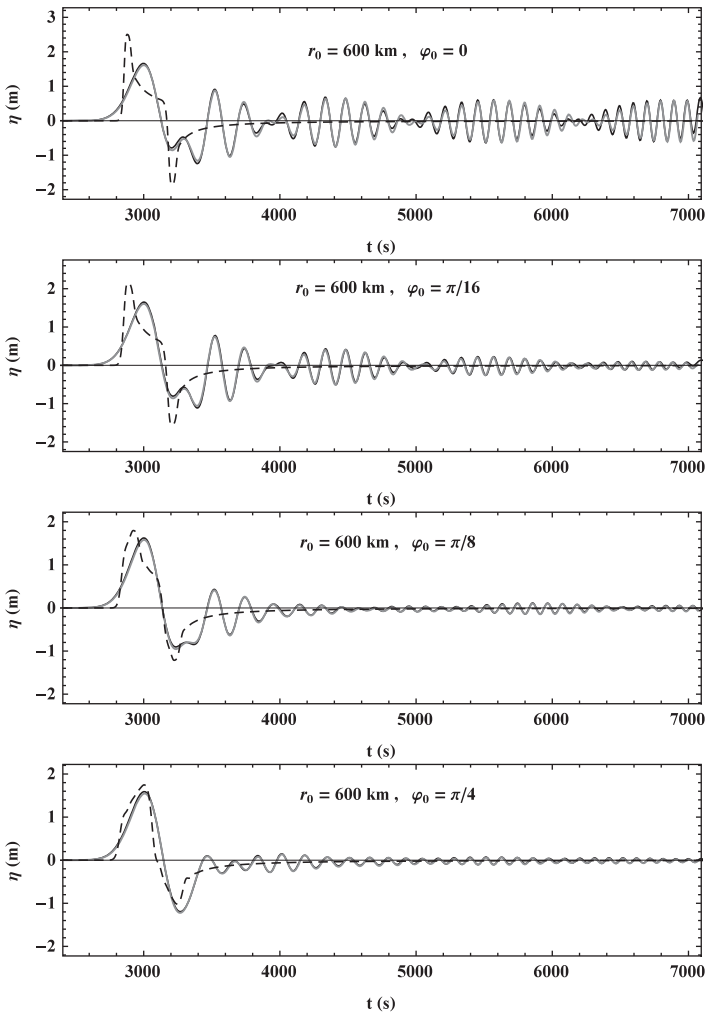

Figure 10. (a–d) Temporal variation of the surface elevation due to an initial square disturbance in 2-D. Results obtained at the observation points defined by equation (84). Gray line, the single convolution summation based on equation (83); black line, results obtained by numerical simulation based on a Boussinesq model; dashed line, numerical simulation based on the linear shallow water equations.

reference solution (as e.g., for $\varphi_0=0$), while it is more accurate if the tail is small (as e.g., for $\varphi_0=\pi/4$).

Figures 11a–11c show the computed temporal variation of the surface elevation at another three locations defined by $\varphi_0=0$, and $r_0 = 400$, 800, and 1200 km, respectively. Small discrepancies between the convolution solution and the linear Boussinesq results can be seen at the first location, while the solutions are almost identical further away from the origin. Again, we can conclude that the uniform asymptotic approximation is very accurate. The linear shallow water model is significantly off at all three locations.

6.3. The Case of an Initial 2-D Gaussian Disturbance

Next, we consider the case of a blunt Gaussian disturbance defined by

$$F[r]=a_2\exp\left[-\frac{r^2}{b_2^2}\right] \quad \text{or}$$
$$F[x,y]=a_2\exp\left[-\left(\frac{x^2+y^2}{b_2^2}\right)\right]. \tag{85}$$

The limiting points A, B, C, and D (see Figure 5) are now located at $(3b_2,\ 3b_2)$, $(3b_2,\ -3b_2)$, $(-3b_2,\ -3b_2)$, and $(-3b_2,\ 3b_2)$ and to obtain the same volume as in the previous square case we choose

$$b_2=\sqrt{\frac{2}{3}}b_1, \quad a_2=\frac{6}{\pi}a_1, \tag{86}$$

with $b_1 = 32$ km, $a_1 = 16$ m, and $h = 4$ km. Convolution covers the initial disturbance area with $n_x = n_y = 100$ grid points in rectangular coordinates and $n_R=n_\theta=100$ grid points in polar coordinates.

With the initial condition being radially symmetric, we now have several options for calculating the impact. First of all, (30) integrates to

$$\Gamma_2[\kappa]=\frac{1}{2}\frac{a_1b_1^2}{h^3}\exp\left[-\frac{b_1^2\kappa^2}{4h^2}\right], \tag{87}$$

which makes it possible to use direct numerical integration of (29). This procedure was recently pursued by *Tobias and Stiassnie* [2011]. Figure 12a shows this solution (full black line) at the observation point $r_0 = 600$ km (i.e., $R_0 = 150$) and $\varphi_0 = \pi/4$. The linear high-order Boussinesq simulation (setup as in the previous square case) is shown as dashed black line. The agreement is outstanding. We have checked the Boussinesq result at other angles but for approximately the same distance, and as expected these results are almost identical due to the axis-symmetry of the source.

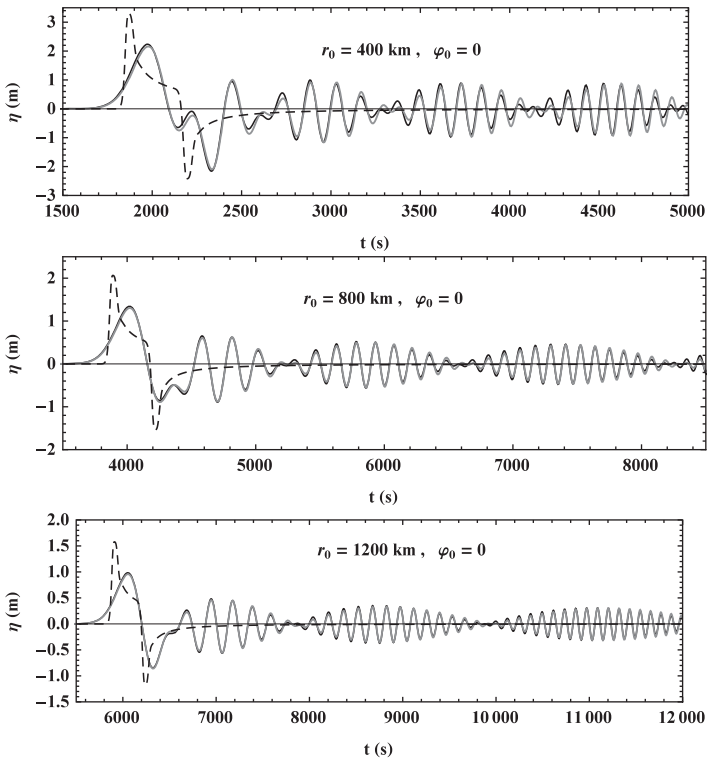

Figure 11. (a–c) Temporal variation of the surface elevation due to an initial square disturbance in 2-D. Description as in Figures 10a–10d.

As a second possibility, we can use convolution by double summation in rectangular coordinates, i.e., (77), convolution by double summation in polar coordinates, i.e., (80) or convolution by single summation, i.e., (83). Generally, these convolution methods are utilizing $\Gamma_{2\delta}=1/(2\pi)$ combined with the uniform approximation ζ_{16} (defined by (71)). As concluded in the previous test case, results obtained by the three different convolution methods are virtually identical and consequently only the single summation results are shown. Figure 12b shows that the uniform convolution solution (dashed line) is in excellent agreement with the direct numerical integration (full line).

Notice that due to the bluntness of the Gaussian disturbance, only a leading wave is seen and the dispersive tail is practically missing. Obviously, this means that there is no need for the full dispersion incorporated in the uniform method. To illustrate this point, we recalculate the single summation convolution with the nonuniform weakly dispersive version of (71), which reads

$$\zeta_{17}[a,\tau]=-\frac{1}{\tau\sqrt{a}}Ai\left[-(1-a)2^{-1/3}\tau^{2/3}\right]Ai'[-(1-a)2^{-1/3}\tau^{2/3}].$$

Figure 12c shows that this result is also in excellent agreement with (29).

As a final possibility, we can use ζ_{16} (defined by (71)) directly as an analytical expression with Γ_2, defined by (87) and evaluated at the stationary points $\kappa=\kappa_0$. This is by far the fastest method for Gaussian disturbances. However, Figure 12d shows that it leads to a significant overestimate and phase-shift of the leading wave compared to the direct numerical integration. This may come as a surprise considering that *Berry* [2005] found excellent agreement with numerical integration in all his test cases. The reason is, however, that Berry only considered very narrow Gaussian shapes. With the present, much wider, Gaussian shape, the accuracy of this procedure is poor, although it gradually improves with increasing distances from the event. For the present source, we have found that this method overestimates the peak of the leading wave by 60% for $r_0=600$ km, 32% for $r_0=1200$ km, 19% for $r_0=2400$ km, 14% for $r_0=3600$ km, and 10% for $r_0=6000$ km.

Even though the relatively wide Gaussian disturbance generates a transient wave with almost no dispersive tail in the near field (as seen in Figures 12a–12d), the dispersive tail will gradually grow during the propagation over large distances. To illustrate this point, Figures 13a–13c show a comparison of the different solutions at the observation point $r_0=6000$ km (i.e., $R_0=1500$) and $\varphi_0=\pi/4$. Figure 13a shows again an excellent agreement between the direct numerical integration and the single summation convolution combined with the uniform expression ζ_{16}. In contrast, Figure 13b shows that the single summation convolution combined with the nonuniform expression ζ_{17} starts to become

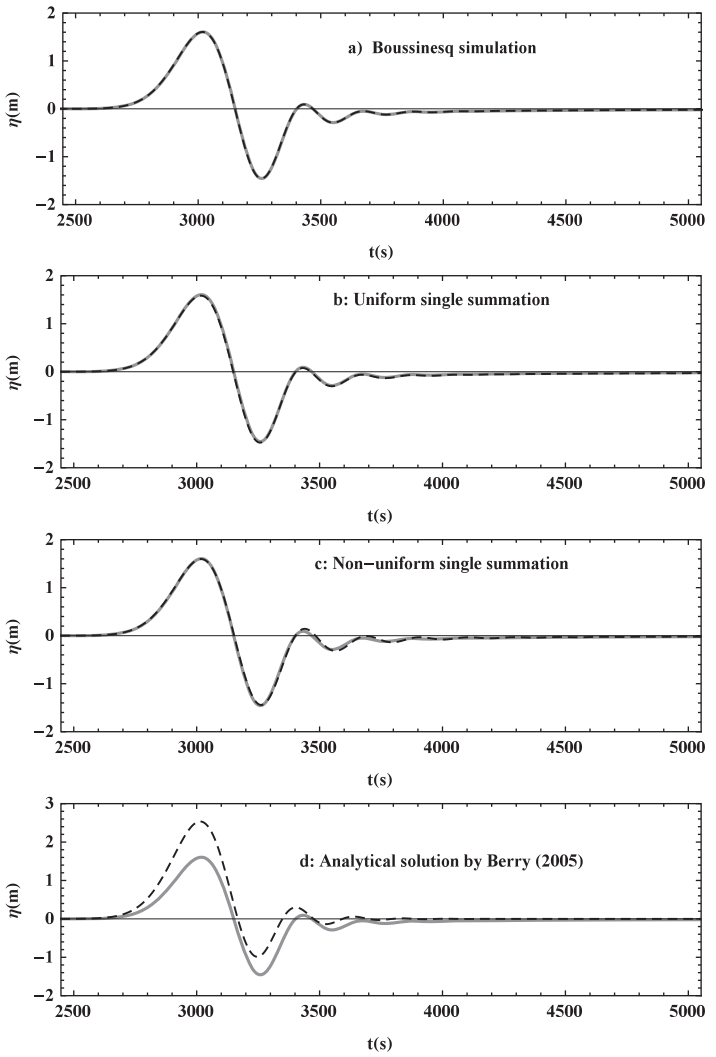

Figure 12. (a–d) Temporal variation of the surface elevation due to an initial Gaussian disturbance in 2-D. Results are obtained at the location $r_0 = 600$ km from the center of the initial disturbance on a constant depth of $h = 4$ km. All figures show the direct integral solution as a full gray line. This is compared to the numerical Boussinesq simulation in Figure 12a (black dashed); the uniform single summation convolution in Figure 12b (black dashed); the corresponding nonuniform single summation convolution in Figure 12c (black dashed); and the direct analytical solution in Figure 12d (black dashed).

inaccurate. Finally, Figure 13c shows that the direct use of (71) with (87) starts to become more accurate, but even with such a large distance to the event discrepancies can still be seen. We therefore do not recommend this method. Speedwise the direct numerical integration takes about 200–400 s, while the single summation convolution (83) takes about 3–5 s.

7. Convolution Formulation for Geophysical Problems

7.1. Extension of the Convolution Method to an Uneven Bottom

Geophysical large-scale problems call for a number of modifications of the methods presented so far, partly because the waves propagate on the surface of a sphere, and partly because the water depth is not constant.

The first issue is related to distances on a curved surface and it is easily incorporated in the model: locations are typically defined in spherical coordinates, e.g., longitude/latitude degrees (θ, φ) and the radius of the Earth ($R_E = 6{,}371{,}000$ m). These are related to the Cartesian coordinate system by

$$(x,\, y,\, z) = R_E(\cos[\varphi\cos\theta,\ \ \cos\varphi\sin\theta,\ \ \sin\varphi]). \tag{88}$$

The shortest curved distance between two locations (A and O) on the sphere is along the segment of the great circle joining them and it is determined by

$$r_{AO} = \phi_{AO} R_E, \tag{89}$$

where ϕ_{AO} defines the angle ACO (in radians) with C being the center of the sphere. This angle is determined by

$$\cos[\phi_{AO}] = \cos[\varphi_A]\cos[\varphi_O]\cos[\theta_A - \theta_O] + \sin[\varphi_A]\sin[\varphi_O]. \tag{90}$$

The second issue is related to geometrical spreading and it is also easily incorporated in the model: for a disturbance radiating from a point source on a flat surface, the conservation of energy flux along the perimeter of the expanding circle will make the wave amplitude decay with the distance to the power $-1/2$. This feature is clearly incorporated in (71). However, when the disturbance moves on a sphere, the effective perimeter of

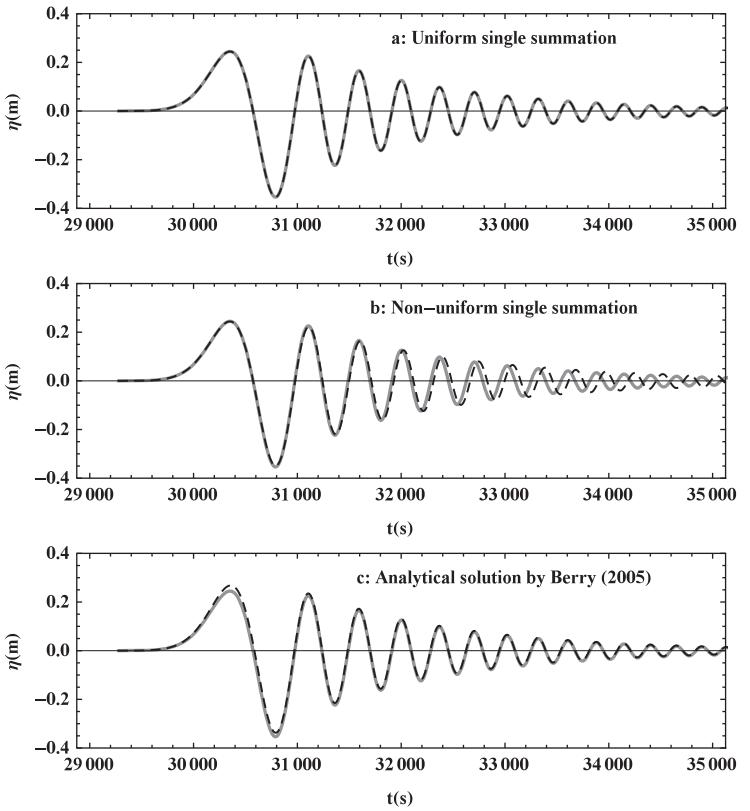

Figure 13. (a–c) Temporal variation of the surface elevation due to an initial Gaussian disturbance in 2-D. Results are obtained at the location $r_0 = 6000$ km from the center of the initial disturbance on a constant depth of $h = 4$ km. All figures show the direct integral solution as a full gray line. This is compared to the uniform single summation convolution in Figure 13a (black dashed); the corresponding nonuniform single summation convolution in Figure 13b (black dashed); and the direct analytical solution in Figure 13c (black dashed).

the small circle will be $2\pi R_E \sin[\phi_{AO}]$ rather than $2\pi r_{AO}$ and therefore the response function (71) needs to be multiplied by the spreading factor

$$\alpha_{AO} = \sqrt{\frac{\phi_{AO}}{\sin[\phi_{AO}]}}. \tag{91}$$

The third, and most important, issue is related to the fact that the water depth $h[\theta, \varphi]$ is generally not constant and as a result shoaling, refraction, and diffraction may be important. Diffraction can only be incorporated for idealized canonical bathymetries and even in this case it is not a trivial task [see e.g., *Berry*, 2007]. Refraction is also very difficult to incorporate as it would require that we track each radiating beam from source to observation point. We have therefore chosen to ignore refraction/diffraction and focus on the incorporation of linear shoaling and its influence on the travel time of the leading wave.

As a starting point, we assume that each discrete source point (A) will result in a wave disturbance travelling along a straight transect of the bathymetry from A to the relevant observation point O. This is obviously a crude approximation, which may be violated in case of refraction (and diffraction). We resolve the transect with typically $N = 300$–500 discrete points and integrate the linear shallow water celerity to obtain the following estimate of the arrival time (travel time) of the first disturbance

$$t_{AO} = \frac{r_{AO}}{N} \sum_{j=0}^{N} \frac{1}{\sqrt{gh[\theta_j,\ \varphi_j]}}, \tag{92}$$

where

$$\theta_j \equiv \theta_O + \frac{j}{N}(\theta_A - \theta_O), \quad \varphi_j \equiv \varphi_O + \frac{j}{N}(\varphi_A - \varphi_O). \tag{93}$$

The corresponding mean water depth (d_{AO}) associated with each transect is now determined from

$$\sqrt{g d_{AO}} = \frac{r_{AO}}{t_{AO}}. \tag{94}$$

Finally, linear shoaling along each transect is approximated by Green's law, i.e.,

$$\beta_{AO} = \left(\frac{h[\theta_O, \varphi_O]}{h[\theta_A, \varphi_A]}\right)^{-1/4}. \tag{95}$$

We emphasize that this approach is based on nondispersive linear shallow water theory. This is to some extent justified by the fact that natural tsunami sources often appear with relatively mild spatial

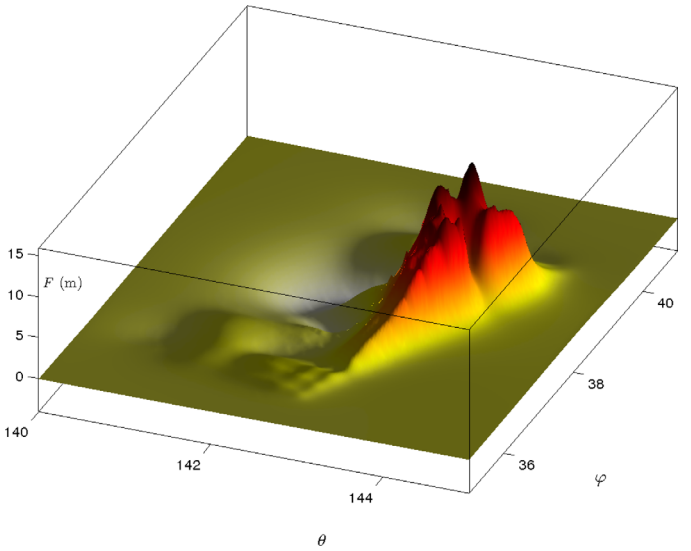

Figure 14. Perspective plot of the UCSB source from the 2011 Tohoku tsunami in Japan.

gradients leading to relatively weak dispersion in the leading waves. With this in mind, there is no reason to expect that the resulting uneven bottom version of the uniform asymptotic approximation will perform any better than a version based on the classical nonuniform asymptotic approximation. At this point, our goal is simply to investigate the ability of these models to predict the leading waves of the geophysical tsunami.

The fourth issue is the grid resolution of the source region: This is typically given in longitude/latitude degrees as

$$\Delta\theta=\left(\frac{\theta_{\max}-\theta_{\min}}{n_\theta-1}\right),\quad \Delta\varphi=\left(\frac{\varphi_{\max}-\varphi_{\min}}{n_\varphi-1}\right), \tag{96}$$

and we need to convert it, first to meters and second by normalizing with the mean water depth. This leads to

$$\Delta X=\frac{\gamma\Delta\theta}{d_{AO}}\cos\left[\varphi_A\right],\quad \Delta Y=\frac{\gamma\Delta\varphi}{d_{AO}},\gamma=\frac{2\pi R_E}{360}. \tag{97}$$

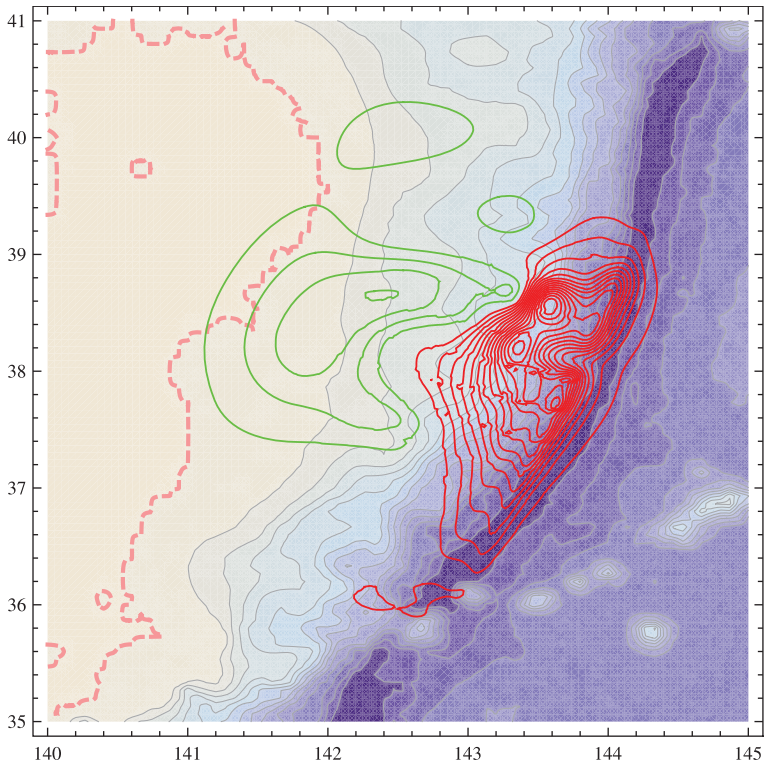

Figure 15. The local bathymetry with an overlay of contours from the UCSB source from the 2011 Tohoku tsunami in Japan. Positive/negative source values shown as red/green contours.

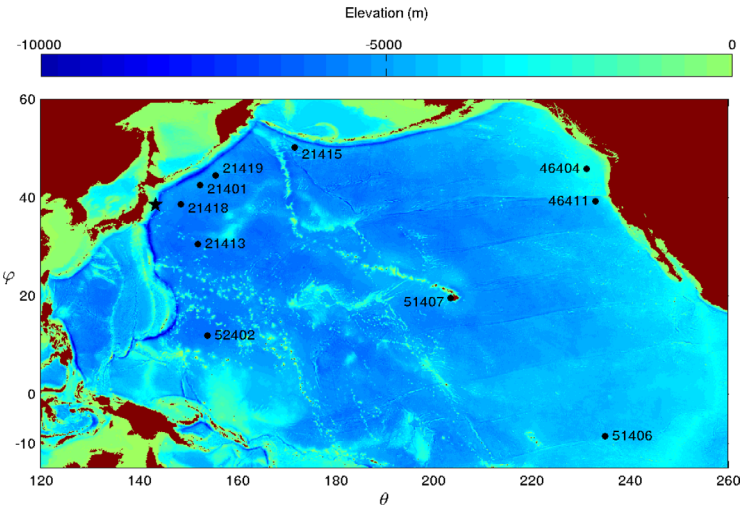

Figure 16. The Pacific including location of DART measurements. Source region indicated as a star.

Note that (89)–(97) should be applied in each discrete source point A with coordinates (θ_A, φ_A) to provide maps of, e.g., distance, travel time, mean depth, spreading index, shoaling index, and local grid resolution for any specific choice of the observation point O. As a consequence, we modify the original source map F_A as follows

$$F_{AO} = \frac{\gamma^2 \Delta\theta \Delta\varphi \cos[\varphi_A]}{d_{AO}^2} \alpha_{AO} \beta_{AO} F_A. \tag{98}$$

The impulse-response function ζ_{16} was defined by (71) as a function of R and τ, but fundamentally it is a function of a and τ. On a constant depth, a is defined as

$$a = \frac{R}{\tau}, \quad \text{where } R = \frac{r}{h_0} \text{ and } \tau = t\sqrt{\frac{g}{h_0}},$$

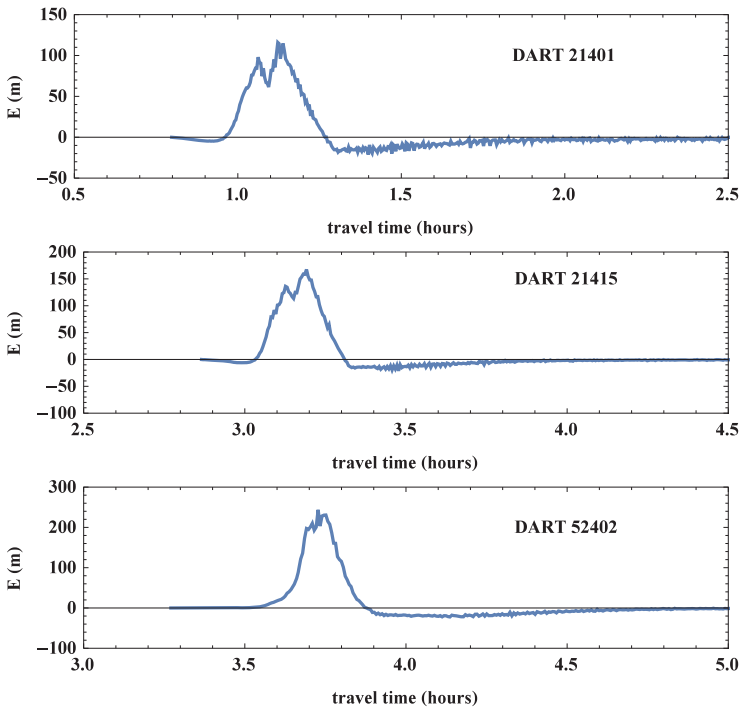

Figure 17. The accumulated source as a function of travel time for DART 21401, 21415, and 52402. E is determined by equation (102).

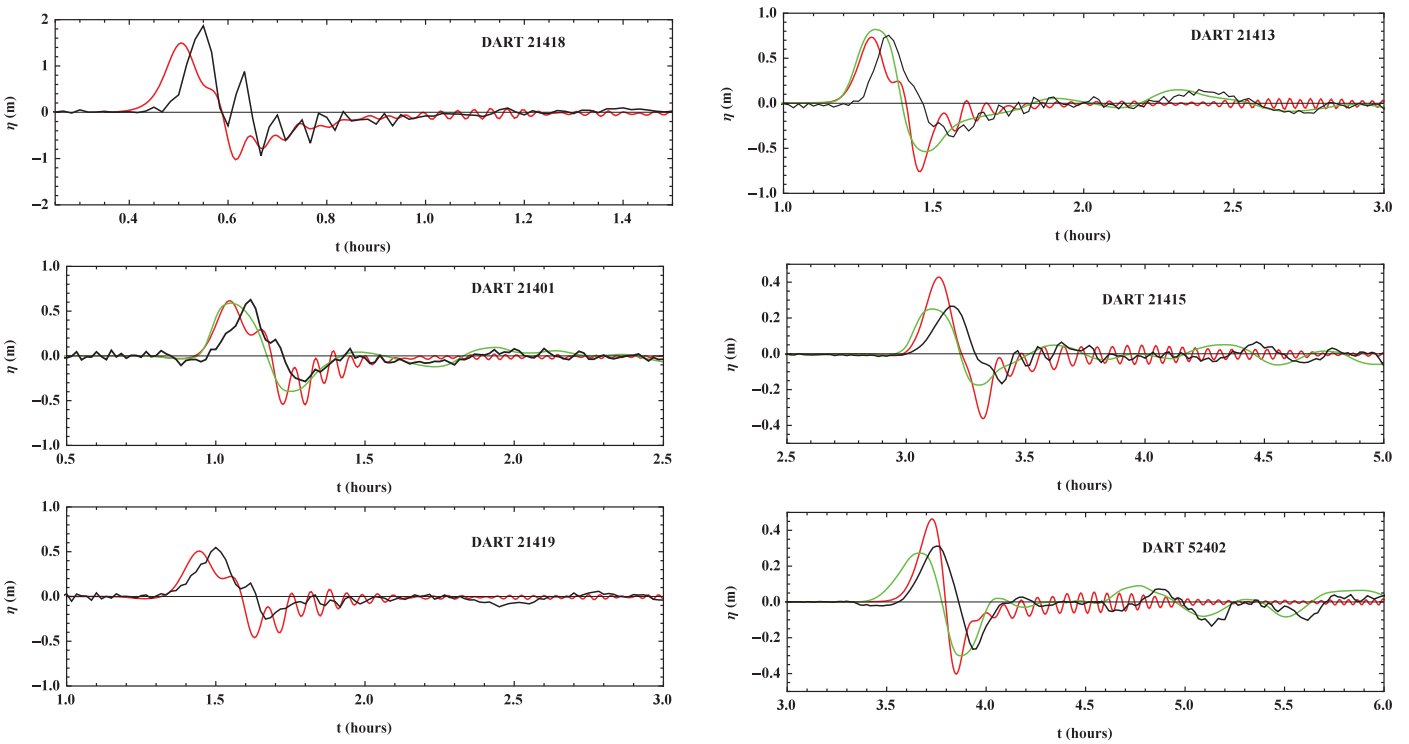

Figure 18. (a–f) Surface elevation at near-field DART buoys due to the 2011 Tohoku tsunami. Black, DART measurements; red, single summation convolution; and green, numerical simulation based on the NSW equations.

but on an uneven bottom, we replace h_0 by d_{AO} and r by r_{AO}, which leads to

$$a[\theta_A, \varphi_A, t] = \frac{t_{AO}[\theta_A, \varphi_A]}{t}, \quad \text{and } \tau[\theta_A, \varphi_A, t] = t\sqrt{\frac{g}{d_{AO}[\theta_A, \varphi_A]}}. \tag{99}$$

On this basis, we modify the double summation convolution (77) to

$$\eta_O[t] = \sum_{\theta_A=\theta_{\min}}^{\theta_{\max}} \sum_{\varphi_A=\varphi_{\min}}^{\varphi_{\max}} F_{AO}[\theta_A, \varphi_A] \;\; \zeta_{16}[a, \;\; \tau], \tag{100}$$

where a and τ are determined by (99) and where $\eta_O[t]$ is the resulting surface elevation (in meters) at the observation point O.

As long as the conversion from t to τ depends on the local mean depth d_{AO} in the source area, we cannot simplify the double summation convolution to a single summation convolution. However, often the variation of d_{AO} is quite limited, and if this is the case we can use the approximation

$$\tau[t] \simeq t\sqrt{\frac{g}{d_{AO}[\theta_{peak}, \varphi_{peak}]}}, \tag{101}$$

where $(\theta_{peak}, \varphi_{peak})$ defines the location of the peak source. This leads to the following simplifications: first, we consider the map of associated $\{t_{AO}, F_{AO}\}$ values representing arrival time and source values at all discrete source points. Second, we cover the interval from $t_{\min}$ to $t_{\max}$ by increments of $\triangle s$ and sum up all F_{AO}-values falling within these discrete Δs-bins. This leads to the accumulated source function

$$E[s] = \sum F_{AO}[s], \quad \text{where } t_{\min} \le s \le t_{\max}. \tag{102}$$

The resulting single summation convolution reads

$$\eta_O[t] = \sum_{s=t_{\min}}^{t_{\max}} E[s]\ \zeta_{16}\left[\frac{s}{t}, \tau\right], \tag{103}$$

where τ is given by (101). Again, this is an extremely fast procedure which can provide the resulting time series in a matter of seconds.

7.2. Applications on the 2011 Japan Tsunami

In order to test the validity of our convolution approach extended to uneven bottom, we study the 2011 Japan tsunami. For this purpose, we have chosen to apply the UCSB source by *Shao et al.* [2011] covering the longitude/latitude area of $140^\circ \le \theta_A \le 145^\circ$ and $35^\circ \le \varphi_A \le 41^\circ$ with 40,000 grid points. *Ren et al.* [2013] used the same source for their simulations with a model based on the nonlinear shallow water (NSW) equations, and their results make a good benchmark in combination with the variety of deep water DART measurements in the Pacific.

The UCSB source is instantaneously triggered at 2.46 P.M. JST (05.46 UTC) on 11 March 2011. The maximum elevation specified by this source is 15.88 m and occurs at $(\theta_{peak}, \varphi_{peak}) = (143.593,\ 38.5578)$. Figure 14 shows a perspective plot of the UCSB source given in meters as a function of the longitude/latitude coordinates, while Figure 15 shows the local bathymetry in the source region with the overlay of the source contours. As observation points, we consider the following deep water DART buoys: 21418, 21401, 21419, 21413, 21415, 52402, 51407, 46404, 46411, and 51406, which are located as indicated in Figure 16. For each of these observation points, the procedure defined by (89)–(101) is executed. As an example, Figures 17a–17c show the modified and accumulated source E determined by (102) and (98) as a function of the travel time to the observation points DART 21401, 21415, and 52402. Generally, we have used double summation as well as single summation convolution and there is hardly any difference for these cases, so only the single summation results are shown in the following.

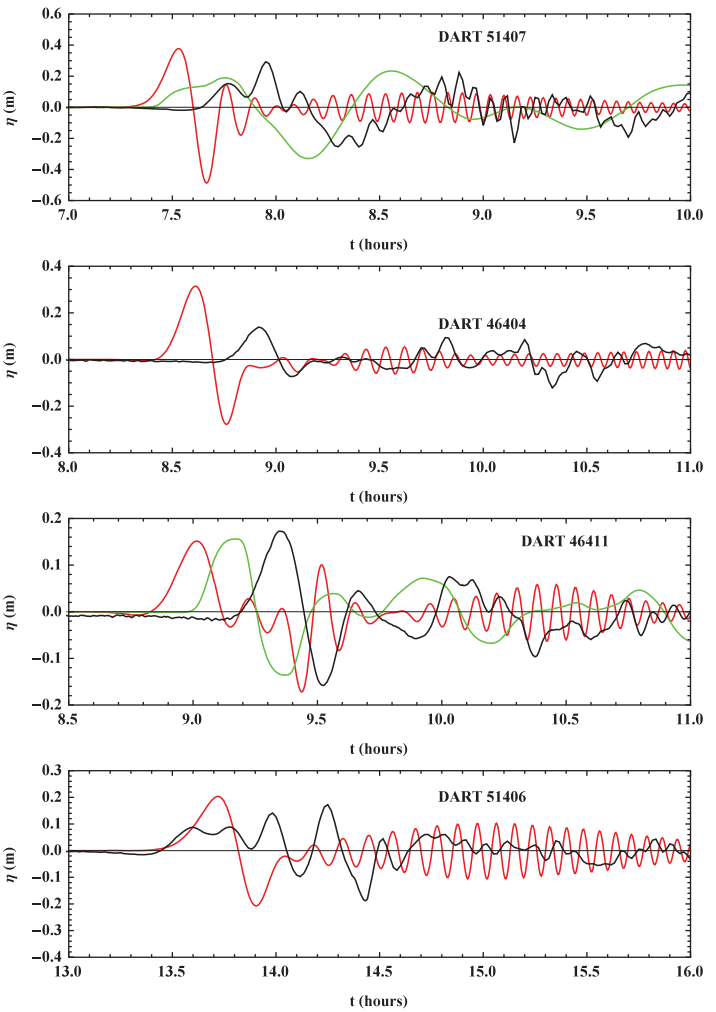

Figure 19. (a–d) Surface elevation at the far-field DART buoys due to the 2011 Tohoku tsunami. Black, DART measurements; red, single summation convolution; and green, numerical simulation based on the NSW equations.

Figures 18a–18f focus on the near-field DART bouys 21418, 21401, 21419, 21413, 21415, and 52402, which are reached by the tsunami within 0.5–3.5 h of travel time. Observations (black) are compared with the convolution results (red) and the NSW simulations (green) by *Ren et al.* [2013]. In stations 21401 and 21413, the two models agree quite well and they are both in pretty good agreement with the measurements. In stations 21415 and 52402, the amplitude of the leading

wave tends to be overestimated by the convolution model, while it is smaller in the NSW simulations and thus in better agreement with the measurements. This trend is in contrast to our earlier comparison of the two models involving propagation on a constant depth (see Figures 10a–10d and 11a–11c). We assume that the reason is refraction effects, which are omitted in the convolution method. The arrival times of the two models are almost the same and typically slightly earlier than the observations. Overall, we may conclude that both models are applicable in the near field.

Figures 19a–19d focus on the far-field DART bouys 51407, 46404, 46411, and 51406, which are reached by the tsunami within 7.5–14 h of travel time. At stations 51407 and 46411, the convolution calculations (red) and the NSW simulations (green) deviate significantly in amplitude as well as in arrival time, and both are quite different from the measurements (black). The fact that the two calculations deviate so much again implies again that refraction (diffraction) effects cannot be ignored in the far field. The convolution approach assumes that disturbances travel along transects connecting the source points and the observation points, and while this is correct on a flat bottom it is not necessarily a good approximation on a uneven bottom, where waves may take different paths. Furthermore, due to refraction, a wave signal radiating in all directions from a point source may arrive at the observation point from several directions and with different time lags, and this is again not taken into account by the convolution model. We conclude that the convolution model is not applicable in the far field if significant refraction and diffraction effects are present.

On the other hand, it should also be emphasized that the far-field NSW model results are far from impressive. *Løvholt et al.* [2012] used a different source distribution and achieved much better agreement, e.g., at location 51407. They modeled the Tohoku tsunami with a linear weakly dispersive Boussinesq model and a linear nondispersive shallow water model and both sets of results were generally found to be superior to the results by *Ren et al.* [2013]. This clearly implies that the UCSB source used in the present work is not sufficiently accurate.

8. Summary and Conclusion

In this work, we have presented a semianalytical method for the linear and fully dispersive propagation of waves over constant depth due to an initial surface displacement. In the first part (sections 2–4), we have rederived impulse-response functions for the 1-D and 2-D linear Cauchy-Poisson problem on a constant depth. The derivation utilizes integral formulations combined with the method of stationary phase, the method of uniform approximations, and various Airy integral formulations. The resulting formulation is very efficient and highly accurate, incorporating full dispersion.

In the second part (sections 5 and 6), we have presented three different convolution techniques in order to deal with initial surface elevations of arbitrary shape on a constant depth. The most efficient of these techniques effectively reduces the 2-D problem to a 1-D problem and determines the solution within a few seconds on a standard desktop computer. The procedure is first tested on a 1-D rectangular disturbance and a 2-D square disturbance. Both events are sharp edged and generate a transient wave with a highly dispersive tail, and they are therefore well suited to test the dispersion properties of the uniform asymptotic approximations. Results are compared to numerical simulations with a linearized high-order Boussinesq model, and the agreement is found to be excellent. In comparison, numerical simulations with the linear shallow water model fail to capture the dispersive tail as well as the temporal development of the leading waves.

Second, we consider the case of a wide Gaussian disturbance in 2-D, which allows for a direct numerical integration, a direct analytical formulation, and three different convolution formulations. In the near field, this case will result in transient waves dominated by a single leading wave and with almost no dispersive tail. This implies that the classical nonuniform and weakly dispersive formulations of *Kajiura* [1963] and *Whitham* [1974] will do acceptably for this case, which is confirmed by our calculations. In the far field, however, the dispersive tail will grow and the nonuniform formulation will start to become inaccurate. Hence, we conclude that even for rather blunt disturbances, dispersion will eventually play a role. We conclude that the proposed single summation convolution method combined with the uniform asymptotic impulse-response function is superior in terms of flexibility, speed, and accuracy for linear fully dispersive transient problems on a constant depth.

Finally, we have made a first effort to extend the convolution method to geophysical problems (section 7). Various effects associated with the motion on a sphere and the motion over an uneven bottom have been incorporated. Of these, the uneven bottom is by far the most problematic to incorporate. In our extension, we have

neglected refraction/diffraction while approximating shoaling via linear shallow water theory. This leads to fairly simple estimates of travel time and travel paths connecting the source and observation points by straight transects. The modified convolution procedure has been tested on data from the 2011 Japan tsunami from 10 DART buoys in the Pacific and it has been compared to NSW simulations based on the same tsunami source. It turns out that results agree fairly well with observations within the near field, i.e., for locations within 0.5–3.5 h of travel time. It is, however, also clear that far-field results (within 7.5–14 h) are quite poor: the travel time is clearly underestimated and the time signals deviate from observations as well as from the NSW simulations. We conclude that far-field locations are quite sensitive to refraction (and diffraction) effects, which make the disturbances travel along a diversity of paths before reaching the observation point. Such effects are important to recognize, though they are unfortunately beyond the reach of the present convolution procedure.

Acknowledgments

The following contributions to this work are highly appreciated: M. V. Berry and J.-M. Clarisse clarified various aspects of their original works from 2005 and 1995 via several email communications. Hua Liu and Zhiyuan Ren kindly provided data from their study of the Japan 2011 tsunami. D. R. Fuhrman acknowledges support from the European Union project ASTARTE, grant 603839 (FP7-ENV-2013.6.4-3). The DART measurements can be obtained from the NOAA site www.ndbc.noaa.gov/dart.shtml. All remaining data used in this paper can be obtained by e-mail request to the first author at prm@mek.dtu.dk.

References

Berry, M. V. (2005), Tsunami asymptotics, *New J. Phys.*, *7*, 129.
Berry, M. V. (2007), Focused tsunami waves, *Proc. R. Soc. A*, *463*, 3055–3071.
Bleistein, N. (1966), Uniform asymptotic expansion of integrals with stationary point and nearby algebraic singularity, *Commun. Pure Appl. Math.*, *19*, 353–370.
Bleistein, N. (1967), Uniform asymptotic expansions of integrals with many nearby stationary points and algebraic singularities, *J. Math. Mech.*, *17*(6), 533–559.
Chester, C., B. Friedman, and F. Ursell (1957), An extension of the method of steepest descents, *Proc. Cambridge Philos. Soc.*, *53*, 599–611.
Child, M. S. (1975), A uniform approximation for one-dimensional matrix elements, *Mol. Phys.*, *29*, 1421–1429.
Clarisse, J.-M., J. N. Newman, and F. Ursell (1995), Integrals with a large parameter: Water waves on finite depth due to an impulse, *Proc. R. Soc. London, Ser. A*, *450*, 67–87.
Fuhrman, D. R., and H. B. Bingham (2004), Numerical solutions of fully nonlinear and highly dispersive Boussinesq equations in two horizontal dimensions, *Int. J. Numer. Methods Fluids*, *44*, 231–255.
Glimsdal, S., G. K. Pedersen, H. P. Langtangen, V. Shuvalov, and H. Dypvik (2007), Tsunami generation and propagation from the Mjølnir asteroid impact, *Meteorit. Planet. Sci.*, *42*(9), 1473–1493.
Glimsdal, S., G. K. Pedersen, C. B. Harbitz, and F. Løvholt (2013), Dispersion of tsunamis: Does it really matter?, *Nat. Hazard Earth Syst. Sci.*, *13*, 1507–1526.
Grilli, S.T., J. C. Harris, T. S. T. Bakhsh, T. L. Masterlark, C. Kyriakopoulos, J. T. Kirby, and F. Shi (2013), Numerical simulation of the 2011 Tohoku tsunami based on a new transient FEM co-seismic source: Comparison to far- and near-field observations, *Pure Appl. Geophys.*, *170*, 1333–1359.
Kajiura, K. (1963), The leading wave of a tsunami, *Bull. Earthquake Res. Inst. Univ. Tokyo*, *41*, 525–571.
Kuznetsov, N. (2006), Asymptotic analysis of rapid forward accelerations of a free-surface pressure, *J. Eng. Math.*, *55*, 167–181.
Lamb, H. (1932), *Hydrodynamics*, 6th ed., Cambridge Univ. Press.
LeBlond, P. H., and L. A. Mysak (1978), *Waves in the Ocean*, Elsevier, N. Y.
Løvholt, F., S. Kaiser, S. Glimsdal, L. Scheele, C. B. Harbitz, and G. Pedersen (2012), Modelling propagation and inundation of the 11 March 2011 Tohoku tsunami, *Nat. Hazard Earth Syst. Sci.*, *12*, 1017–1028.
Madsen, P. A. and H. A. Schäffer (2010), Analytical solutions for tsunami runup on a plane beach: single waves, N-waves and transient waves, *J. Fluid Mech.*, *645*, 27–57.
Madsen, P. A., H. B. Bingham, and H. Liu (2002), A new Boussinesq method for fully nonlinear waves from shallow to deep water, *J. Fluid Mech.*, *462*, 1–30.
Madsen, P. A., D. R. Fuhrman, and H. A. Schäffer (2008), On the solitary wave paradigm for tsunamis, *J. Geophys. Res.*, *113*, C12012, doi: 10.1029/2008JC004932.
Newman, J. N. (1991), Asymptotic approximations of the Cauchy-Poisson problem, in *Mathematical Approaches in Hydrodynamics*, pp. 225–237, SIAM, Philadelphia, Pa.
Ren, Z., B. Wang, T. Fan, and H. Liu (2013), Numerical analysis of impacts of 2011 Japan Tohoku tsunami on China Coast, *J. Hydrodyn.*, *25*(4), 580–590.
Sekerzh-Zenkovich, S. Y. (2009), Simple asymptotic solution of the Cauchy-Poisson problem for head waves, *Russ. J. Math. Phys.*, *16*(2), 315–322.
Shao, G., X. Li, C. Ji, and T. Maeda (2011), Focal mechanism and slip history of 2011 M_w 9.1 off the Pacific coast of Tohoku Earthquake, constrained with teleseismic body and surface waves, *Earth Planets Space*, *63*, 559–564.
Stokes, G. G. (1850), On the numerical calculation of a class of definite integrals and infinite series, *Trans. Cambridge Philos. Soc.*, *9*, 166–187.
Tang, L., et al. (2012), Direct energy estimation of the 2011 Japan tsunami using deep-ocean pressure measurements, *J. Geophys. Res.*, *117*, C08008, doi:10.1029/2011JC007635.
Thomson, W. (1887), On the waves produced by a single impulse in water of any depth, or in a dispersive medium, *Philos. Mag.*, *23*, 252–255.
Tobias, J., and M. Stiassnie (2011), An idealized model for tsunami study, *J. Geophys. Res.*, *116*, C06026, doi:10.1029/2010JC006763.
Ursell, F. (1965), Integrals with a large parameter. The continuation of uniformly asymptotic expansions, *Proc. Cambridge Philos. Soc.*, *61*, 113–128.
Ursell, F. (1980), Integrals with a large parameter: A double complex integral with four nearly coincident saddle-points, *Math. Proc. Cambridge Philos. Soc.*, *87*, 249–273.
Ursell, F. (2007), Water wave problems, their mathematical solution and physical interpretation, *J. Eng. Math.*, *58*, 7–17.
Vallée, O., and M. Soares (2004), *Airy Functions and Applications to Physics*, World Sci., Singapore.
Wehausen, J. V. and E. V. Laitone (1960), Surface waves, in *Encyclopedia of Physics*, vol. 9, pp. 446–778.
Whitham, G. B. (1974), *Linear and Nonlinear Waves*, Wiley-Interscience, N. Y.
Wong, R. (1989), *Asymptotic Approximations of Integrals*, Academic, N. Y.